SIAM J. IMAGING SCIENCES
Vol. 17, No. 3, pp. 1690–1728

Three-Stage Approach for 2D/3D Diffeomorphic Multimodality Image Registration with Textural Control*

Ke Chen† and Huan Han‡

Abstract. Intensity inhomogeneity is a challenging task in image registration. Few past works have addressed the case of intensity inhomogeneity due to texture noise. To address this difficulty, we propose a novel three-stage approach for 2D/3D diffeomorphic multimodality image registration. The proposed approach contains three stages: (1) $H^{-1}+H^0+H^2$ decomposition which decomposes the image pairs into texture, noise, and smooth component; (2) Blake–Zisserman homogenization which transforms the geometric features from different modalities into approximately the same modality in terms of the first-order and second-order edge information; (3) image registration which combines the homogenized geometric features and mutual information. Based on the proposed approach, the greedy matching for multimodality image registration is discussed and a coarse-to-fine algorithm is also proposed. Furthermore, several numerical tests are performed to validate the efficiency of the proposed approach.

Key words. multimodality, intensity inhomogeneity, image decomposition, Blake–Zisserman, image registration

MSC codes. 68U10, 94A08, 65K10, 65M12

DOI. 10.1137/23M1583971

1. Introduction.

Image registration is used to search for a spatial transformation such that the deformed image looks like the target image as much as possible. In mathematics, it is formulated in the following way. Given a bounded domain $\Omega \subset \mathbb{R}^d (d = 2, 3)$ with Lipschitz boundary $\partial\Omega$ and two functions/images $T, R : \Omega \to \mathbb{R}$, the goal of diffeomorphic image registration is to search for a bijective deformation $\boldsymbol{\varphi} : \Omega \to \Omega$ such that the deformed floating image $T \circ \boldsymbol{\varphi}(\cdot)$ looks like the target image $R(\cdot)$ as much as possible. For this purpose, the framework for the 2D/3D diffeomorphic image registration is formulated as follows:

$$\min_{\mathbf{u}\in\mathcal{N}} \xi\mathcal{D}(T \circ \boldsymbol{\varphi}(\cdot), R(\cdot)) + \varpi\mathcal{S}(\mathbf{u}), \tag{1.1}$$

*Received by the editors July 5, 2023; accepted for publication (in revised form) May 13, 2024; published electronically July 26, 2024.
https://doi.org/10.1137/23M1583971
Funding: The first author was supported in part by EPSRC (EP/N014499/1). The second author was supported in part by the National Natural Science Foundation of China (11901443), the Natural Science Foundation of Hubei Province of China (2022CFB379), and the National Key Research and Development Program of China (2020YFA0714200).
†Department of Mathematics and Statistics, University of Strathclyde, Glasgow, G1 1XH, UK, and Centre for Mathematical Imaging Techniques, University of Liverpool, Liverpool, L69 7ZL, UK (K.Chen@strath.ac.uk).
‡Corresponding author. Department of Mathematics, Wuhan University of Technology, Wuhan, 430070, People's Republic of China (hanhuan11@whut.edu.cn).

where $\xi, \varpi > 0$, $\mathcal{D}(\cdot,\cdot)$ is the fidelity, and the regularization $\mathcal{S}(\mathbf{u})$ provides some prior estimate on $\mathbf{u}$; here and in what follows, $\boldsymbol{\varphi}(\mathbf{x}) = \mathbf{x} + \mathbf{u}(\mathbf{x})$, and $\mathcal{N}$ is a set which enforces the model (1.1) to produce diffeomorphic deformation.

Concerning the regularization $\mathcal{S}(\mathbf{u})$, different applications may adopt different forms. Many types of $\mathcal{S}(\mathbf{u})$ have been proposed, for instance, total variation (TV) [8], mean curvature [9], Gaussian curvature [26], and fractional-order TV^{α}-L^2 [52]. For the fidelity $\mathcal{D}(\cdot,\cdot)$, one may also have different choices [3, 7, 21, 22, 31, 39, 40] according to whether the image pair $T(\cdot)$ and $R(\cdot)$ are produced by the same imaging technique. Generally, if $T(\cdot)$ and $R(\cdot)$ are of the same type (i.e., CT-CT, MRI-MRI), it is called monomodality image registration. In this case, the sum of squared difference (SSD) [3, 21, 22] is the most popular fidelity for image registration because of its robustness and simple structure. For the case that $T(\cdot)$ and $R(\cdot)$ are of different types of images (i.e., CT-MRI, PET-CT), it is named multimodality image registration. In this case, the intensity difference based SSD no longer works, since the intensity in different modalities is of different physical meanings. To address this problem, some other fidelities are proposed to characterize the similarity of multimodality image pairs, for example, mutual information (MI) [17], the maximum correlation coefficient (MCC) [7], the normalized cross-correlation (NCC) [31], and the normalized gradient fields (NGF) [17]. These fidelities can be classified into two categories: geometric feature based fidelity (GFBF) and intensity based fidelity (IBF). For GFBF, the main advantage is incarnated in registration for images with dominant geometric features. The pioneering work for GFBF is the NGF proposed by Droske and Rumpf [14], who modeled the fidelity by the SSD of the normalized gradients for the image pair. Later on, Haber and Modersitzki [17] improved the NFG by replacing the SSD in [14] with cosine of the normalized gradients for the image pair. Also based on gradient information, Wirth [44] introduced a penalty term to enforce the registration of edges in the segmentation-registration joint problem. As an improvement for gradient-based registration, Theljani and Chen [42] also proposed a new normalized gradient field (NNGF). These works are modeled by using the gradient information. As we all know, due to noise and data imperfection/inconsistency (for example, intensity inhomogeneity for images), it is expected to extract consistent geometric information by a model rather than simply scaling the gradients information. This is specifically important for images whose gradients are not prominent or second-order information is equally useful, for example, *the multimodality registration with intensity inhomogeneity.* In addition, NGF and NNGF pay attention to the deformation for boundaries, and the lack of control for the small scale feature (i.e., texture) may lead to an error in matching for these small scale features. In fact, texture is an important image feature and viewed as a set of primitive texels in some regular or repeated pattern. It is a small scale feature which is modeled as an oscillating component (see section 2.1 for a review of the modeling of texture) and easily destroyed in image processing [34]. For this reason, the registration for textures is challenging. To our knowledge, there seem to be few results for this challenge. *This will be a problem to be addressed in this paper.* Concerning the IBF, the advantage focuses on the characterization of the global intensity correlation between the image pairs. The pioneering work for IBF comes from Maes et al. [29], who modeled the fidelity using MI between the image pairs. Since then, many other fidelities for multimodality image registration have been introduced, for example, MCC [7] and NCC [31]. Though there are many different fidelities, MI is considered the state-of-the-art fidelity for multimodality image registration, although it has a number of well-known disadvantages. The main disadvantage of the MI based registration model lies in the difficulty of estimating the probability density function and the lack of local geometric feature characterization. To improve MI, some new fidelities [35] which combine MI and gradient information are proposed. For these models, the main drawback is the lack of ability to address image registration with intensity inhomogeneity, because the gradient information does not work well for intensity inhomogeneity.

In addition to intensity inhomogeneity and textural control, physical mesh folding [53] is also a key challenge for multimodality image registration. As we know, mesh folding implies the volume vanishing of particles after transformation. This contradicts the physical principle. Therefore, eliminating mesh folding is a key challenge for image registration, especially for medical image registration. Under this framework, deformation $\boldsymbol{\varphi}$ is expected to be a bijection. As we all know, the inverse function theorem [15] provides a sufficient condition for this goal. Generally, it is stated as follows.

Theorem 1.1 (inverse function theorem). *Suppose Ω is a simply connected domain and $\boldsymbol{\varphi} \in C^1(\Omega)$; then $\boldsymbol{\varphi} : \Omega \to \Omega$ is a local bijection (the inverse $\boldsymbol{\varphi}^{-1} \in C^1(\Omega)$ is also a local bijection) if and only if $\det(\nabla\boldsymbol{\varphi}(\mathbf{x})) \neq 0$ for any $\mathbf{x} \in \Omega$.*

In physical view, $\det(\nabla\boldsymbol{\varphi}(\mathbf{x}))$ denotes the volume stretching rate for the transformation $\boldsymbol{\varphi} : \Omega \to \Omega$. Stretching rate is positive. Hence, the condition $\det(\nabla\boldsymbol{\varphi}(\mathbf{x})) \neq 0$ in Theorem 1.1 is replaced by $\det(\nabla\boldsymbol{\varphi}(\mathbf{x})) > 0$ in this article. In addition, by additionally giving the boundary condition $\boldsymbol{\varphi}(\mathbf{x}) = \mathbf{x}$ on $\partial\Omega$ and defining $\boldsymbol{\varphi}(\mathbf{x}) = \mathbf{x}$ if $\mathbf{x} \in \mathbb{R}^d \setminus \Omega$, then $\boldsymbol{\varphi} \in C^1(\mathbb{R}^d)$ with $\lim_{\|\mathbf{x}\|\to+\infty} \|\boldsymbol{\varphi}(\mathbf{x})\| = +\infty$. It follows from the corollary on page 200 in [45] that $\boldsymbol{\varphi} : \mathbb{R}^d \to \mathbb{R}^d$ is a C^1 global diffeomorphism. That is, the local bijection in Theorem 1.1 can be replaced by global bijection if the condition $\boldsymbol{\varphi}(\mathbf{x}) = \mathbf{x}$ on $\partial\Omega$ is added. Under this framework, some diffeomorphic image registration models have been proposed [27, 11, 20, 21, 24, 28, 36, 37, 46, 49, 50]. These models can be mainly classified into three categories: (i) using quasi conformal/conformal theory [27, 20, 21, 24, 37, 46, 49, 50] to control the Beltrami coefficient; (ii) constraining the solution to the set which ensures $\det(\nabla\boldsymbol{\varphi}(\mathbf{x})) > 0$ for each $\mathbf{x} \in \Omega$ [53]; (iii) introducing the stored energy function of an Ogden material [11]. For the first choice, Chun and Lui [27] introduced the quasi-conformal theory to control the mesh folding. Following this work, several models were proposed to improve the quasi-conformal model [48]. Particularly, Han, Wang, and Zhang also gave a series of 2D/3D diffeomorphic image registration models and algorithms by restricting $\mathbf{u}$ into the 2D/3D conformal set [20, 21, 24]. For the second choice, Zhang, Chen, and Yu [53] proposed a diffeomorphic image registration model by restricting the deformation $\boldsymbol{\varphi}$ into a set which ensures $\det(\nabla\boldsymbol{\varphi}(\mathbf{x})) > 0$ for each $\mathbf{x} \in \Omega$. For the third choice, Debroux, Le Guyader, and Vese [11] established a framework of variational methods and hyperelasticity by viewing the shapes to be matched as Ogden materials. The above works for mesh folding mainly focus on the monomodality image registration in which SSD acts as fidelity. To our knowledge, there seem to have been only a few works addressing mesh folding for multimodality, for example, [13, 14, 51]. *This will be a problem to be addressed in this paper.* Though more restrictive compared with quasi-conformal mappings, the 2D/3D conformal set [21] is still selected as the constraint in this paper for the following reasons: it preserves the topological structure of tissue and provides a much simpler constraint for diffeomorphic mappings, which further makes possible the mathematical analysis of the proposed model (i.e., address the greedy matching [23, 24]).

To address the mesh folding, intensity inhomogeneity, and small feature (i.e., texture) control for multimodality image registration, we propose a novel three-stage approach for 2D/3D diffeomorphic multimodality image registration (see section 2 for details). The contribution of this paper is as follows:

- Propose a three-stage approach for 2D/3D diffeomorphic multimodality image registration with intensity inhomogeneity; the proposed approach contains three parts: (I) $H^{-1}+H^0+H^2$ decomposition which decomposes the image pairs into texture, noise, and smooth component. Note that throughout this paper, $H^0 \triangleq L^2$ denotes the Banach space L^2. (II) Blake–Zisserman (B-Z) homogenization which transforms the geometric features from different modalities into the same modality based on texture and smooth component. (III) Image registration which combines the homogenized geometric features and MI.
- Introduce textural control to address the registration for small scale features inside the boundary.
- Discuss greedy matching for the proposed model to provide a more accurate solution.
- Propose a coarse-to-fine algorithm for greedy matching.

Remark 1.2. To make the numerical implementation easier, the proposed three-stage approach is purely sequential to avoid the coupled terms for different stages. In fact, one can also consider some joint works for these three stages, for example, merging Stage 1 and Stage 2 to process jointly the decomposition steps and noticeable characteristic extraction.

The rest of this paper is organized as follows. In section 2, a three-stage approach for 2D/3D diffeomorphic multimodality image registration is proposed and the numerical implementation is also discussed. In section 3, greedy matching for the proposed multimodality image registration model is discussed and a coarse-to-fine algorithm for solving the greedy problem is proposed. In section 4, several numerical tests and comparisons are performed to show the efficiency of the proposed algorithm. Finally, we conclude our paper and list some problems for future research in section 5.

2. Three-stage approach for 2D/3D diffeomorphic multimodality image registration.

To address the intensity inhomogeneity, mesh folding, and textural control in 2D/3D multimodality image registration, we propose a novel three-stage approach for 2D/3D diffeomorphic multimodality image registration. The proposed approach contains image decomposition, B-Z homogenization, and image registration, which will be introduced in the following three subsections, respectively.

2.1. $H^{-1}+H^0+H^2$ decomposition.

Decomposition of an image into smooth, texture, and noisy parts was much studied about 20 years ago based on the seminal work of Meyer [30], but there are few follow-up works to extend the ideas to problems beyond a static image. For image decomposition, it is usually modeled as an inverse problem: given an observed image $U_0:\Omega\to\mathbb{R}$, find another image $U:\Omega\to\mathbb{R}$ and feature $V:\Omega\to\mathbb{R}$ such that U is a cartoon of U_0 and V represents the specific small scale feature. That is, $U_0=U+V$. Generally, V represents noise (random pattern) or texture (oscillate feature). For the case V representing noise, it is not kept. This is so-called noise removal; we refer readers to [6, 33, 38] for details. For the case of V representing texture, it is modeled as an oscillating component for the image. Concerning this topic, the pioneering works were done independently by Meyer [30] and Mumford and Gidas [32], who modeled the texture by introducing the distribution $\mathrm{div}(L^\infty(\Omega,\mathbb{R}^d))$. However, the convex model in [30, 32] cannot be solved directly since the associated Euler–Lagrange equation with respect to U cannot be expressed directly. To overcome this difficulty, Vese and Osher [43] proposed a practical method by adopting $\mathrm{div}(L^p(\Omega,\mathbb{R}^d))(p\geq 1)$ to model the texture. Particularly, by taking $p=2$, the model in [43] induced a classical model which modeled the texture via $H^{-1}(\Omega)=\mathrm{div}(L^2(\Omega,\mathbb{R}^d))$. Motivated by the above works, Shen [41] proposed an $H^{-1}+H^0+H^1$ model to decompose the image into texture, noise, and smooth component. Note that in [41], only the first-order feature and the texture are included. To additionally introduce the second-order feature which will be useful for latter modeling, here we extend the model in [41] to the following $H^{-1}+H^0+H^2$ decomposition model:

$$\min_{U\in H^2(\Omega),V\in H^{-1}(\Omega)} \mathcal{E}(U,V), \tag{2.1}$$

where $\mathcal{E}(U,V)=\alpha_1\int_\Omega|\nabla^2U|^2d\mathbf{x}+\alpha_2\int_\Omega|\nabla U|^2d\mathbf{x}+\mu\int_\Omega|\nabla(-\triangle)^{-1}V|^2d\mathbf{x}+\lambda\int_\Omega(U_0-U-V)^2d\mathbf{x}$, $(-\triangle)^{-1}$ is the inverse of the negative Laplacian operator, and constants $\alpha_1,\alpha_2,\mu,\lambda>0$, and images $U_0,U,V:\Omega\to\mathbb{R}$ are the original image, smooth component, and texture, respectively.

The minimization problem (2.1) involves the Hessian matrix of U denoted by ∇^2U. It appears like an $H^{-1}+H^0+H^1+H^2$ model, establishing its existence and uniqueness can be done in a similar way to the proof of [41]. In particular, we highlight two key steps of the proof for (2.1): (1) show the weak lower semicontinuity of $\mathcal{E}(U,V)$; (2) show the strict convexity of $\mathcal{E}(U,V)$. Here we do not repeat it. The main challenge for the model (2.1) is the texture term $\int_\Omega|\nabla(-\triangle)^{-1}V|^2d\mathbf{x}$. This term forces the texture component V to be an oscillatory function. Therefore, directly solving the $H^{-1}+H^0+H^2$ model (2.1) is faced with the difficulty of numerical instability. To address this difficulty, we introduce a new variable ϕ to relax $(-\triangle)^{-1}V$. That is, $-\Delta\phi\approx V$. Based on this relaxation, (2.1) is reformulated into the following relaxed form:

$$\min_{U\in\mathcal{H},V\in H_0^1(\Omega),\phi\in H_0^2(\Omega)} \mathcal{F}(U,V,\phi), \tag{2.2}$$

where $\mathcal{F}(U,V,\phi)=\alpha_1\int_\Omega|\nabla^2U|^2d\mathbf{x}+\alpha_2\int_\Omega|\nabla U|^2d\mathbf{x}+\mu\int_\Omega|\nabla\phi|^2d\mathbf{x}+\lambda\int_\Omega(U_0-U-V)^2d\mathbf{x}+\beta\int_\Omega|V+\Delta\phi|^2d\mathbf{x}$, $\mathcal{H}=\{U\in H^2(\Omega):U|_{\partial\Omega}=U_0,\ \frac{\partial^l U}{\partial x_i^l}|_{\partial\Omega}=0,\ l=1,2; i=1,\dots,d\}$, $\beta>0$.

Remark 2.1. Intuitively, (2.1) and (2.2) are equivalent if β is large enough (i.e., $\beta\to+\infty$). Therefore, by giving some specific β, (U_β,V_β) produced by (2.2) is only an approximate solution of $H^{-1}+H^0+H^2$ model (2.1). In addition, in the case where the observed image satisfies $U_0|_{\partial\Omega}=0$, $\mathcal{H}$ can be degenerated to $H_0^2(\Omega)$. To avoid too complex discussions of the theoretical analysis of model (2.2), U is restricted into the space $H_0^2(\Omega)$ in the following part for theoretical analysis. In fact, for the case where the observed image does not satisfy $U_0|_{\partial\Omega}=0$, one can extend the region Ω to some larger region $\widetilde{\Omega}$ $(\Omega\subset\widetilde{\Omega})$ with $U_0:\widetilde{\Omega}\to\mathbb{R}$ such that $U_0|_{\partial\widetilde{\Omega}}=0$. By replacing Ω with $\widetilde{\Omega}$ in (2.2), the specific problem is transformed to the case $U_0|_{\partial\Omega}=0$ which will be discussed in the following part.

Letting (U, V, ϕ) be the solution of model (2.2), then (U, V, ϕ) satisfies the following partial differential equation (PDE) in the sense of distribution:

$$\begin{cases} \alpha_1 \Delta^2 U - \alpha_2 \Delta U - \lambda(U_0 - U - V) = 0, \\ -\lambda(U_0 - U - V) + \beta(V + \Delta\phi) = 0, \\ -\mu\Delta\phi + \beta\Delta(V + \Delta\phi) = 0, \end{cases} \tag{2.3}$$

with boundary condition $U|_{\partial\Omega} = U_0|_{\partial\Omega} = 0$, $\frac{\partial^l U}{\partial x_i^l}|_{\partial\Omega} = 0$ $(l = 1, 2; i = 1, \ldots, d)$, $V|_{\partial\Omega} = 0$, $\phi|_{\partial\Omega} = 0$.

Eliminating ϕ using the second and the third equation in (2.3) leads to the following equivalent PDE:

$$\begin{cases} \alpha_1 \Delta^2 U - \alpha_2 \Delta U - \lambda(U_0 - U - V) = 0, \\ -\lambda\Delta V + \gamma V - \theta(U_0 - U) + \lambda\Delta(U_0 - U) = 0, \end{cases} \tag{2.4}$$

where $\theta = \frac{\mu\lambda}{\beta}$, $\gamma = \mu + \theta$.

Giving some initial guess U^0 and V^0, (2.4) may be solved by the following alternating minimization method (AMM):

$$\begin{cases} \alpha_1 \Delta^2 U^{k+1} - \alpha_2 \Delta U^{k+1} - \lambda(U_0 - U^{k+1} - V^k) = 0, \\ -\lambda\Delta V^{k+1} + \gamma V^{k+1} - \theta(U_0 - U^{k+1}) + \lambda\Delta(U_0 - U^{k+1}) = 0, \end{cases} \tag{2.5}$$

where $k = 0, 1, 2, \ldots$.

Furthermore, by (2.3) and (2.4), AMM (2.5) is equivalent to the following three subproblems:

$$U^{k+1} = \arg\min_{U \in H_0^2(\Omega)} \mathcal{F}(U, V^k, \phi^k), \tag{2.6}$$

$$V^{k+1} = \arg\min_{V \in H_0^1(\Omega)} \mathcal{F}(U^{k+1}, V, \phi^k), \tag{2.7}$$

$$\phi^{k+1} = \arg\min_{\phi \in H_0^2(\Omega)} \mathcal{F}(U^{k+1}, V^{k+1}, \phi). \tag{2.8}$$

Based on (2.6)–(2.8), we give the convergence results of the AMM (2.5).

Theorem 2.2. *The sequence $\{(U^k, V^k)\}$ induced by AMM (2.5) converges (strongly in $L^2(\Omega) \times L^2(\Omega)$ and weakly in $H_0^2(\Omega) \times H_0^1(\Omega)$) to the solution of (2.4) as $k \to +\infty$.*

Proof. Giving a small number $\varepsilon > 0$ and setting some perturbation $\varepsilon\tilde{U} \in H_0^2(\Omega)$ along U in the subproblem (2.6), then there holds

$$\begin{aligned} &\frac{d\mathcal{F}(U^{k+1} + \varepsilon\tilde{U}, V^k, \phi^k)}{d\varepsilon}\Big|_{\varepsilon=0} \\ &= 2\alpha_1 \int_\Omega \nabla^2 U^{k+1} \cdot \nabla^2 \tilde{U} d\mathbf{x} + 2\alpha_2 \int_\Omega \nabla U^{k+1} \cdot \nabla\tilde{U} d\mathbf{x} - 2\lambda \int_\Omega (U_0 - U^{k+1} - V^k) \cdot \tilde{U} d\mathbf{x} = 0 \end{aligned} \tag{2.9}$$

for any $\tilde{U} \in H_0^2(\Omega)$.

Taking $\tilde{U} = U^k - U^{k+1}$ in (2.9), then we have that

$$\tilde{L}_1 = \alpha_1 \int_\Omega \nabla^2 U^{k+1} \cdot \nabla^2 (U^k - U^{k+1}) d\mathbf{x} + \alpha_2 \int_\Omega \nabla U^{k+1} \cdot \nabla (U^k - U^{k+1}) d\mathbf{x} \tag{2.10}$$
$$- \lambda \int_\Omega (U_0 - U^{k+1} - V^k) \cdot (U^k - U^{k+1}) d\mathbf{x} = 0.$$

In addition, there holds

$$\mathcal{F}(U^k, V^k, \phi^k) - \mathcal{F}(U^{k+1}, V^k, \phi^k) = \alpha_1 \|\nabla^2 U^k - \nabla^2 U^{k+1}\|^2_{L^2(\Omega)} + \alpha_2 \|\nabla U^k - \nabla U^{k+1}\|^2_{L^2(\Omega)} \tag{2.11}$$
$$+ \lambda \|U^k - U^{k+1}\|^2_{L^2(\Omega)} + \tilde{L}_1 \geq c_1 \|U^k - U^{k+1}\|^2_{H_0^2(\Omega)}$$

for some $c_1 = \min(\alpha_1, \alpha_2, \lambda)$. Note that here we use the fact $\tilde{L}_1 = 0$ in (2.10).

In a similar way, one can also know that

$$\mathcal{F}(U^{k+1}, V^k, \phi^k) - \mathcal{F}(U^{k+1}, V^{k+1}, \phi^k) = (\lambda + \beta) \|V^k - V^{k+1}\|^2_{L^2(\Omega)} \geq c_2 \|V^k - V^{k+1}\|^2_{L^2(\Omega)} \tag{2.12}$$

and

$$\mathcal{F}(U^{k+1}, V^{k+1}, \phi^k) - \mathcal{F}(U^{k+1}, V^{k+1}, \phi^{k+1})$$
$$= \mu \|\nabla \phi^k - \nabla \phi^{k+1}\|^2_{L^2(\Omega)} + \beta \|\Delta \phi^k - \Delta \phi^{k+1}\|^2_{L^2(\Omega)}$$
$$\geq c_3 \|\phi^k - \phi^{k+1}\|^2_{H_0^1(\Omega)} + \beta \|\Delta \phi^k - \Delta \phi^{k+1}\|^2_{L^2(\Omega)} \tag{2.13}$$

for some $c_2, c_3 > 0$.

Following (2.11), (2.12), and (2.13), we obtain that

$$a_k - a_{k+1} \triangleq \mathcal{F}(U^k, V^k, \phi^k) - \mathcal{F}(U^{k+1}, V^{k+1}, \phi^{k+1})$$
$$\geq c_1 \|U^k - U^{k+1}\|^2_{H_0^2(\Omega)} + c_2 \|V^k - V^{k+1}\|^2_{L^2(\Omega)} + c_3 \|\phi^k - \phi^{k+1}\|^2_{H_0^1(\Omega)}$$
$$+ \beta \|\Delta \phi^k - \Delta \phi^{k+1}\|^2_{L^2(\Omega)}, \tag{2.14}$$

where $a_k \triangleq \mathcal{F}(U^k, V^k, \phi^k) \in \mathbb{R}$.

It follows from (2.14) that $\{a_k\}_{k=0}^\infty$ is a decreasing sequence with lower bound. Therefore, there exists $a \in \mathbb{R}$ such that $\lim_{k\to\infty} a_k = a$ and $a_k \geq a$ $\forall k \in \mathbb{N}$. This implies

$$\|U^k - U^{k+1}\|_{H_0^2(\Omega)} \xrightarrow{k} 0, \ \|V^k - V^{k+1}\|_{L^2(\Omega)} \xrightarrow{k} 0 \tag{2.15}$$

and

$$\|\phi^k - \phi^{k+1}\|_{H_0^1(\Omega)} \xrightarrow{k} 0, \ \|\triangle \phi^k - \triangle \phi^{k+1}\|_{L^2(\Omega)} \xrightarrow{k} 0 \tag{2.16}$$

as k goes to infinity.

By (2.9), there holds

$$\int_\Omega [\alpha_1 \triangle^2 U^{k+1} - \alpha_2 \triangle U^{k+1} - \lambda (U_0 - U^{k+1} - V^k)] \tilde{U} d\mathbf{x} = 0,$$

and it is reformulated as

$$\int_\Omega [\alpha_1 \triangle^2 U^{k+1} - \alpha_2 \triangle U^{k+1} - \lambda(U_0 - U^{k+1} - V^{k+1})]\tilde{U}\, d\mathbf{x} = \int_\Omega \lambda(V^{k+1} - V^k)\tilde{U}\, d\mathbf{x}. \tag{2.17}$$

By using the Holder's inequality and (2.15), we have that

$$\left| \int_\Omega (V^{k+1} - V^k)]\tilde{U}\, d\mathbf{x} \right| \leq \|V^{k+1} - V^k\|_{L^2(\Omega)} \|\tilde{U}\|_{L^2(\Omega)} \xrightarrow{k} 0, \tag{2.18}$$

as k goes to infinity.

It follows from (2.17) and (2.18) that $\alpha_1 \triangle^2 U^{k+1} - \alpha_2 \triangle U^{k+1} - \lambda(U_0 - U^{k+1} - V^{k+1})$ goes to 0 as $k \to +\infty$, in the sense of distribution.

Giving a small number $\varepsilon > 0$ and setting some perturbation $\varepsilon \tilde{V} \in H_0^1(\Omega)$, $\varepsilon \tilde{\phi} \in H_0^2(\Omega)$ along V and ϕ in the subproblem (2.7) and (2.8), respectively, there holds

$$\begin{aligned} &\frac{d\mathcal{F}(U^{k+1}, V^{k+1} + \varepsilon \tilde{V}, \phi^k)}{d\varepsilon}\Big|_{\varepsilon=0} \\ &= 2\int_\Omega [-\lambda(U_0 - U^{k+1} - V^{k+1}) + \beta(V^{k+1} + \Delta\phi^k)]\tilde{V}\, d\mathbf{x} = 0 \end{aligned} \tag{2.19}$$

and

$$\begin{aligned} &\frac{d\mathcal{F}(U^{k+1}, V^{k+1}, \phi^{k+1} + \varepsilon\tilde{\phi})}{d\varepsilon}\Big|_{\varepsilon=0} \\ &= 2\mu \int_\Omega \nabla \phi^{k+1} \cdot \nabla\tilde{\phi} d\mathbf{x} + 2\beta \int_\Omega (V^{k+1} + \Delta\phi^{k+1})\Delta\tilde{\phi} d\mathbf{x} = 0 \end{aligned} \tag{2.20}$$

for any $\tilde{V} \in H_0^1(\Omega), \tilde{\phi} \in H_0^2(\Omega)$.

(2.19) is reformulated as

$$\int_\Omega [-\lambda(U_0 - U^{k+1} - V^{k+1}) + \beta(V^{k+1} + \Delta\phi^{k+1})]\tilde{V}\, d\mathbf{x} = \beta \int_\Omega (\triangle\phi^{k+1} - \triangle\phi^k) \cdot \tilde{V}\, d\mathbf{x} \xrightarrow{k} 0, \tag{2.21}$$

because $|\int_\Omega (\triangle\phi^{k+1} - \Delta\phi^k) \cdot \tilde{V}\, d\mathbf{x}| \leq \|\triangle\phi^{k+1} - \triangle\phi^k\|_{L^2(\Omega)} \|\tilde{V}\|_{L^2(\Omega)} \xrightarrow{k} 0$ as k goes to infinity.

That is,

$$-\lambda(U_0 - U^{k+1} - V^{k+1}) + \beta(V^{k+1} + \Delta\phi^{k+1}) \to 0, \tag{2.22}$$

as k goes to infinity in the sense of distribution.

By (2.14), $\alpha_1 \|\nabla^2 U^k\|^2_{L^2(\Omega)} + \alpha_1 \|\nabla U^k\|^2_{L^2(\Omega)} + \mu\|\nabla\phi^k\|^2_{L^2(\Omega)} \leq \mathcal{F}(U^k, V^k, \phi^k) \leq \mathcal{F}(U^0, V^0, \phi^0) \triangleq \tilde{M}$. This concludes U^k (or ϕ^k) is bounded in $H_0^2(\Omega)$ (or $H_0^1(\Omega)$) and thus compact in $L^2(\Omega)$ [15], we can extract a subsequence of U^k (or ϕ^k) which is labeled by U^{n_k} (or ϕ^{n_k}) such that U^{n_k} (or ϕ^{n_k}) strongly converges to some $U \in L^2(\Omega)$ (or $\phi \in L^2(\Omega)$), and we may also assume $\nabla^2 U, \nabla U$ (or $\nabla^2\phi, \nabla\phi$) are the weak limits of $\nabla^2 U^{n_k}, \nabla U^{n_k}$ (or $\nabla^2\phi^{n_k}, \nabla\phi^{n_k}$), respectively.

Based on these notations, from (2.22), there holds

$$V^{k+1} = \frac{\lambda(U_0 - U^{k+1}) - \beta\triangle\phi^{k+1}}{\lambda+\beta} \xrightarrow{k} \frac{\lambda(U_0 - U) - \beta\triangle\phi}{\lambda+\beta} \tag{2.23}$$

in the sense of distribution.

That is, there exists some $V = \frac{\lambda(U_0-U)-\beta\triangle\phi}{\lambda+\beta} \in L^2(\Omega)$ such that $V^{k+1} \xrightarrow{k} V$, which implies

$$-\lambda(U_0 - U - V) + \beta(\triangle\phi + V) = 0. \tag{2.24}$$

Furthermore, we claim that

$$\alpha_1\triangle^2 U - \alpha_2\triangle U - \lambda(U_0 - U - V) = 0. \tag{2.25}$$

To show the claim (2.25), we define $\mathcal{A}(\psi) = \alpha_1\triangle^2\psi - \alpha_2\triangle\psi$ and $\mathcal{T} = \lambda(U_0 - U - V)$. As $\mathcal{A}$ is the derivative of a convex functional, it is a monotone operator and we can write

$$(\mathcal{A}(U^{n_k}) - \mathcal{A}(\psi), U^{n_k} - \psi) \geq 0 \tag{2.26}$$

for any $\psi \in H_0^2(\Omega)$.

As $k \to +\infty$,

$$\begin{aligned}(\mathcal{A}(\psi), U^{n_k}) &= \int_\Omega \alpha_1\nabla^2\psi\cdot\nabla^2 U^{n_k} + \alpha_2\nabla\psi\cdot\nabla U^{n_k}\, d\mathbf{x} \\ &\to \int_\Omega \alpha_1\nabla^2\psi\cdot\nabla^2 U + \alpha_2\nabla\psi\cdot\nabla U\, d\mathbf{x} = (\mathcal{A}(\psi), U),\end{aligned} \tag{2.27}$$

as $\nabla^2 U^{n_k}$ and ∇U^{n_k} converge to $\nabla^2 U$ and ∇U, weakly in $L^2(\Omega)$, respectively.

Furthermore, by the fact that $\alpha_1\triangle^2 U^{k+1} - \alpha_2\triangle U^{k+1} - \lambda(U_0 - U^{k+1} - V^{k+1})$ goes to 0, we have

$$(\mathcal{A}(U^{n_k}), U^{n_k}) = \lambda\int_\Omega (U_0 - U^{n_k} - V^{n_k})U^{n_k}\, d\mathbf{x} + \lambda\int_\Omega (V^{n_k} - V^{n_k-1})U^{n_k}\, d\mathbf{x} \tag{2.28}$$

goes to $(\mathcal{T}, U)$ using the strong convergence of U^{n_k}.

By (2.26)–(2.28), we have that

$$(\mathcal{T} - \mathcal{A}(\psi), U - \psi) \geq 0. \tag{2.29}$$

Taking $\psi = U + \tau\chi$ for any $\tau > 0$ and any $\chi \in C_c^\infty(\Omega)$, (2.29) is reformulated as

$$(\mathcal{T} - \mathcal{A}(U + \tau\chi), \chi) \leq 0. \tag{2.30}$$

That is,

$$(\mathcal{T}, \chi) \leq (\mathcal{A}(U), \chi). \tag{2.31}$$

Therefore, $\mathcal{T} = \mathcal{A}(U)$, which concludes the claim (2.25).

In a similar way, one can show

$$\mu\triangle\phi+\beta\triangle(V+\Delta\phi)=0. \tag{2.32}$$

By (2.24) and (2.25), we know (U,V) is the solution of (2.3) and (2.4). ■

The first equation in (2.5) is a fourth-order PDE whose numerical implementation is faced with numerical instability. To overcome this difficulty, we introduce a new variable $\psi^{k+1}=-\Delta U^{k+1}$. (2.5) is approximated by the alternating minimization method

$$\begin{cases} -\alpha_1\Delta\psi^{k+1}+\alpha_2\psi^{k+1}=\lambda(U_0-U^k-V^k), \\ -\Delta U^{k+1}=\psi^{k+1}, \\ -\lambda\Delta V^{k+1}+\gamma V^{k+1}=\theta(U_0-U^{k+1})-\lambda\Delta(U_0-U^{k+1}), \end{cases} \tag{2.33}$$

by giving some initial guess U^0,V^0,ψ^0 with $k=0,1,2,\ldots$, and the three PDEs in (2.33) are all of the type $-\gamma\Delta U(\mathbf{x})+e(\mathbf{x})U(\mathbf{x})=f(\mathbf{x})$ *whose numerical implementation can be realized as in Appendix* C.

Taking the Barbara image (Figure 1(a)) as an example, where we set Figure 1(a) to be U_0, the smooth component $U(\cdot)$ and texture $V(\cdot)$ produced by model (2.33) are given in Figures 1(b) and 1(c), respectively. One can see that the proposed model (2.33) is efficient in texture extraction. In addition, to compare the proposed model (2.33) with the $H^{-1}+H^0+H^1$ model in [41], we perform the same numerical test on the $H^{-1}+H^0+H^1$ model [41]. The results are given in Figures 1(e)–1(g). By comparing the peak signal to noise ratio (PSNR) [19], we see that the proposed model achieves nearly the same smooth result of the $H^{-1}+H^0+H^1$ model. Note that, compared with the $H^{-1}+H^0+H^1$ model [41], the proposed $H^{-1}+H^0+H^2$ model additionally provides the possibility to extract the second-order feature. This is important for the case where the second-order feature also plays a dominant role.

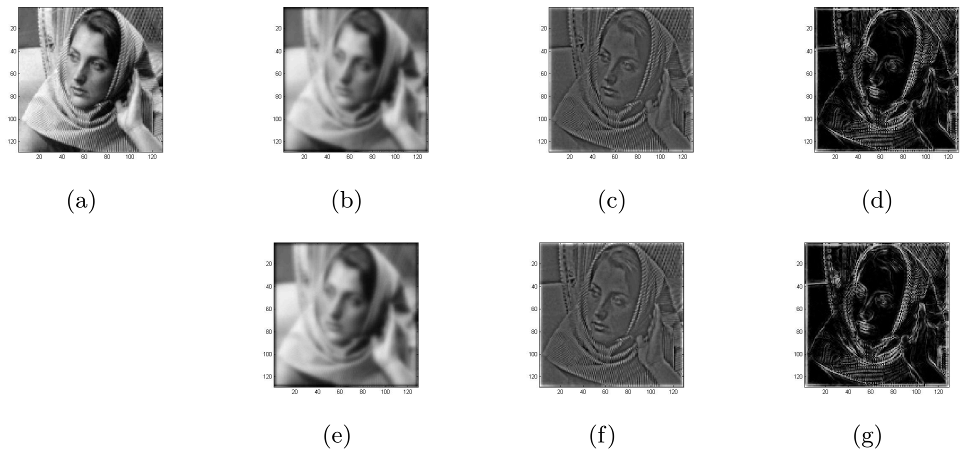

Figure 1. (a) $U_0(\cdot)$; (b) *smooth component* $U(\cdot)$ *by* (2.33), $PSNR=43.73$; (c) *texture* $V(\cdot)$ *by* (2.33); (d) *homogenized texture* $W(\cdot)$ *by* (2.33); (e) *smooth component* $U(\cdot)$ *by Shen's model* [41], $PSNR=42.16$; (f) *texture* $V(\cdot)$ *by Shen's model* [41]; (g) *homogenized texture* $W(\cdot)$ *of* $V(\cdot)$ *in Shen's model* [41].

Setting $U_0 = T$ and $U_0 = R$ in (2.33), one can obtain the smooth component-texture (U_T, V_T), (U_R, V_R) of T and R, respectively. Note these two groups of images will be set as the initial input in the next stage.

2.2. Blake–Zisserman homogenization. To design the fidelity for multimodality image registration, we have a choice of statistic ones [29] and NGF [17, 42] types. Due to noise and intensity inhomogeneity, we wish to extract consistent geometric information by a model rather than simply scaling their gradients. This is specifically important for images whose gradients are not prominent or second-order information is equally useful. In addition, NGF [17] and NNGF [42] pay attention to the deformation for boundaries. The lack of control for the small scale features (i.e., texture) may lead to error in matching for these small scale features. To address these difficulties, our solution is modeling the geometric feature by the following B-Z [1, 4, 5, 47] type functional:

$$\min_{(Z,\omega,W)\in[H^1(\Omega)]^3} \mathcal{B}(Z,\omega,W), \tag{2.34}$$

where $\mathcal{B}(Z,\omega,W) = \mathcal{F}_1(Z) + \mathcal{F}_2(\omega) + \mathcal{F}_3(W)$, $\mathcal{F}_1(Z) = \tau_1 \int_\Omega (Z-1)^2 |\nabla^2 U|^2 d\mathbf{x} + \theta_1 \int_\Omega \varepsilon |\nabla Z|^2 + \frac{1}{4\varepsilon} Z^2 d\mathbf{x}$, $\mathcal{F}_2(\omega) = \tau_2 \int_\Omega (\omega-1)^2 |\nabla U|^2 d\mathbf{x} + \theta_2 \int_\Omega \varepsilon |\nabla \omega|^2 + \frac{1}{4\varepsilon}\omega^2 d\mathbf{x}$, $\mathcal{F}_3(W) = \tau_3 \int_\Omega (W-1)^2 |\nabla V|^2 d\mathbf{x} + \theta_3 \int_\Omega \varepsilon |\nabla W|^2 + \frac{1}{4\varepsilon} W^2 d\mathbf{x}$, $\tau_i, \theta_i > 0$ $(i = 1,2,3)$, and $\varepsilon > 0$ is a small number. Note that here ω, Z, W represent the homogenized first-order discontinuity, second-order discontinuity, and texture feature for the original image U_0, respectively.

Remark 2.3. Three comments are due for (2.34):

(i). One can notice that in the minimization problem (2.34), the first term in $\mathcal{F}_i(\Psi)$ $(\Psi = Z, \omega, W; i = 1,2,3)$ enforces the final result Ψ to be close to 1 at the points $\mathbf{x}$ where the geometric features are discontinuous, and the second term in $\mathcal{F}_i(\Psi)$ enforces Ψ to be close to 0 at the points $\mathbf{x}$ in flat region. In this way, the geometric features are uniformly rescaled into the same type even if $T(\cdot)$ and $R(\cdot)$ are of different modalities. This is the main motivation for us to introduce the B-Z functional in multimodality image registration.

(ii). The reason for introducing the H^2-structure in Stage 1 is the necessity of extracting the second-order discontinuity features in Stage 2. It is used only for the purpose of smoothing the image (similar to the convolution operation). Though it may induce some blur (e.g., Figure 1(b)), it has little influence on extracting the discontinuous feature.

(iii). One can notice that $V \in L^2(\Omega)$ in Stage 1, but ∇V is used in (2.34) to extract the edge of texture. Here we want to emphasis that V in Stage 2 is the smooth version (i.e., texture convolutes some Gaussian kernel) of texture V in Stage 1. This smoothing process may help to extend the width of some thin texture and capture the texture with very thin thickness.

Let (Z,ω,W) be the solution of (2.34). Then by the variational principle [15], there holds

$$\begin{cases} \mathcal{A}_1 Z = 4\varepsilon\tau_1 |\nabla^2 U|^2, \\ \mathcal{A}_2 \omega = 4\varepsilon\tau_2 |\nabla U|^2, \\ \mathcal{A}_3 W = 4\varepsilon\tau_3 |\nabla V|^2, \end{cases} \tag{2.35}$$

where $\mathcal{A}_1 = -4\varepsilon^2\theta_1\Delta + (4\varepsilon\tau_1|\nabla^2 U|^2 + \theta_1)$, $\mathcal{A}_2 = -4\varepsilon^2\theta_2\Delta + (4\varepsilon\tau_2|\nabla U|^2 + \theta_2)$, $\mathcal{A}_3 = -4\varepsilon^2\theta_3\Delta + (4\varepsilon\tau_3|\nabla V|^2 + \theta_3)$.

Concerning the existence and uniqueness of the solution to (2.34) and (2.35), we have the following results.

Theorem 2.4. *Assume* $\operatorname{ess\,sup}_{\mathbf{x}\in\Omega} |\nabla^2 U(\mathbf{x})|^2 < \bar{M} < +\infty$, $\operatorname{ess\,sup}_{\mathbf{x}\in\Omega} |\nabla U(\mathbf{x})|^2 < \bar{M} < +\infty$, $\operatorname{ess\,sup}_{\mathbf{x}\in\Omega} |\nabla V(\mathbf{x})|^2 < \bar{M} < +\infty$ *for some* $M > 0$*; then there exists a unique solution for PDE* (2.35)*.*

Proof. Define $\bar{\mathcal{F}}_1(Z,\tilde{Z}) = \int_\Omega 4\theta_1\varepsilon^2\nabla Z\cdot\nabla\tilde{Z}d\mathbf{x} + \int_\Omega[4\varepsilon\tau_1|\nabla^2 U|^2 + \theta_1]Z\cdot\tilde{Z}d\mathbf{x}$; then there holds

$$
\begin{aligned}
|\bar{\mathcal{F}}_1(Z,\tilde{Z})| &\le 4\theta_1\varepsilon^2\|\nabla Z\|_{L^2(\Omega)}\|\nabla\tilde{Z}\|_{L^2(\Omega)} + [4\varepsilon\bar{M}\tau_1 + \theta_1]\|Z\|_{L^2(\Omega)}\|\tilde{Z}\|_{L^2(\Omega)} \\
&\le C_1\|Z\|_{H^1(\Omega)}\|\tilde{Z}\|_{H^1(\Omega)}
\end{aligned}
\tag{2.36}
$$

for some constant C_1.

Furthermore, we have that

$$
\bar{\mathcal{F}}_1(Z,Z) = 4\theta_1\varepsilon^2\|\nabla Z\|^2_{L^2(\Omega)} + \int_\Omega[\theta_1 + 4\varepsilon\tau_1\|\nabla^2 U\|^2]Z^2 d\mathbf{x} \ge C_2\|Z\|^2_{H^1(\Omega)}
\tag{2.37}
$$

for some $C_2 > 0$.

By (2.36)–(2.37) and Lax–Milgram theorem [10], there exists a unique solution for the first PDE in (2.35).

In a similar way, one can show that there exists a unique solution for the second and the third PDE in (2.35). This concludes Theorem 2.4. ∎

The three PDEs in (2.35) are all of the type $-\gamma\Delta U(\mathbf{x}) + e(\mathbf{x})U(\mathbf{x}) = f(\mathbf{x})$ *whose numerical implementation can be found in Appendix* C. Using (2.35), we draw the homogenized texture feature for the Barbara image (Figure 1(d)). One can notice that Figure 1(d) gives an accurate characterization of the texture distribution for the Barbara image. Furthermore, to show the efficiency of model (2.1) and (2.34), we select a square (Figure 2(a)) and Pineapple-Pepper (Figure 3(a)) as test images. By setting Figures 2(a) and 3(a) to be U_0, the geometric features extracted by model (2.1) and (2.34) are shown in Figures 2(b)–2(c) and Figures 3(b)–3(c), respectively. In addition, to validate the advantage of models (2.1) and (2.34), we also use the NGF [17] to detect the boundary of Figure 2(a), and the result is shown in Figure 2(d). By the comparison between Figures 2(c) and 2(d), one can see that the second-order feature produced

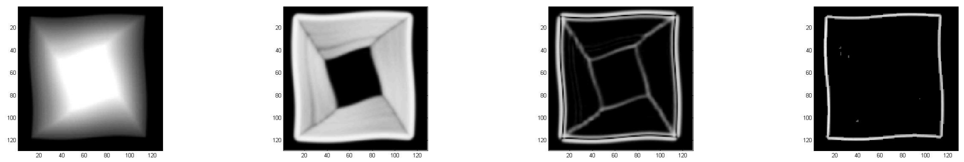

(a) (b) (c) (d)

Figure 2. (a) $U_0(\cdot)$. (b) *First-order feature* Z *by* (2.34). (c) *Second-order feature* ω *by* (2.34). (d) *Boundary detected by NGF.*

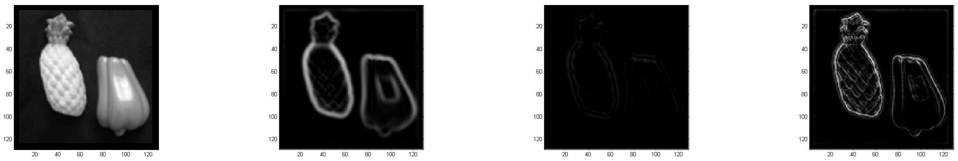

(a) (b) (c) (d)

Figure 3. (a) $U_0(\cdot)$. (b) *First-order feature* Z. (c) *Second-order feature* ω. (d) *Texture* W.

by (2.34) extracts the weak boundary well while the NGF [17] ignores the weak boundary. This advantage provides us the possibility to address the inhomogeneity in multimodality image registration. It is also the main reason why the second-order feature is added in model (2.1) and (2.34). Besides, by the comparison in Figures 2(b) and 2(c), we see that the first-order feature provides much more information inside the boundary; this is our motivation to add a first-order feature in model (2.1) and (2.34). Moreover, it follows from the comparison in Figure 3(b)–(d) that the first-order feature and second-order feature do not extract the texture inside the boundary while the texture W produced by (2.34) succeeds in extracting the texture with very thin thickness. It will be a very useful control for the registration inside the boundary of the object. This is the main motivation why the textural control is additionally introduced in our model. In fact, the textural control is a novelty of the proposed model (2.1) and (2.34) compared with the NGF [17] and NNGF [42] for the multimodality image registration.

Setting $(U,V)=(U_T,V_T)$ and $(U,V)=(U_R,V_R)$, one can solve (2.35) to obtain the homogenized geometric feature Z_T,ω_T,W_T and Z_R,ω_R,W_R, respectively. These homogenized features will be the initial input for the 2D/3D image registration model in the next stage.

2.3. Novel 2D/3D diffeomorphic multimodality image registration. Based on the homogenized geometric features Z_T,ω_T,W_T and Z_R,ω_R,W_R extracted by (2.34), respectively, for the given image pair $T(\cdot)$ and $R(\cdot)$, we propose the following geometric similarity:

$$\begin{aligned}\mathfrak{g}(\mathbf{u}) = {} & \delta_Z\|Z_T\circ\boldsymbol{\varphi}(\cdot)-Z_R(\cdot)\|^2_{L^2(\Omega)}+\delta_\omega\|\omega_T\circ\boldsymbol{\varphi}(\cdot)-\omega_R(\cdot)\|^2_{L^2(\Omega)}\\ & +\delta_W\|W_T\circ\boldsymbol{\varphi}(\cdot)-W_R(\cdot)\|^2_{L^2(\Omega)},\end{aligned}\tag{2.38}$$

where $\boldsymbol{\varphi}(\mathbf{x})=\mathbf{x}+\mathbf{u}(\mathbf{x})$ and the weights $\delta_\nu>0$ $(\nu=Z,\omega,W)$.

Remark 2.5. $\mathfrak{g}(\mathbf{u})$ is a well-defined similarity because of the existence and uniqueness of the solutions to model (2.1) and (2.34). This is due to Φ_ν $(\Phi=Z,\omega,W,\ \nu=T,R)$ being uniquely determined if T,R, and $\mathbf{u}$ are known. In addition, one can selectively set the weights δ_ν $(\nu=Z,\omega,W)$ according to whether the related features are dominant, for example, in data Pineapple-Pepper (Figure 3(a)), whose texture is dominant, it is suggested that one choose a larger δ_W.

In order to combine the geometric feature and the global intensity correlation, we propose the following 2D/3D diffeomorphic multimodality image registration model:

$$\min_{\mathbf{u}\in\mathcal{N}^M_{d,\varepsilon}(\Omega)}\mathcal{K}(\mathbf{u})=\xi\mathcal{D}(\mathbf{u})+\varpi\mathcal{S}(\mathbf{u}),\tag{2.39}$$

where $\mathcal{D}(\mathbf{u}) = \mathfrak{g}(\mathbf{u})\mathcal{M}(\mathbf{u})$, $\mathcal{M}(\mathbf{u}) = \|1 - MI(T\circ\boldsymbol{\varphi}(\cdot), R(\cdot))\|^2_{L^2(\Omega)}$, $\mathcal{S}(\mathbf{u}) = \int_\Omega |\nabla^\alpha \mathbf{u}|^2 d\mathbf{x}$, the MI for $T\circ\boldsymbol{\varphi}(\cdot)$ and $R(\cdot)$ is $MI(T\circ\boldsymbol{\varphi}(\cdot), R(\cdot)) = \int_{-\infty}^{+\infty}\int_{-\infty}^{+\infty} p_{\boldsymbol{\varphi}}^{T,R}(i_1,i_2)\,\log\frac{p_{\boldsymbol{\varphi}}^{T,R}(i_1,i_2)}{p^R(i_2)p_{\boldsymbol{\varphi}}^T(i_1)}di_1di_2$, $G_\sigma(i_1,i_2) = K_\sigma(i_1)K_\sigma(i_2)$, $K_\sigma(i) = \frac{1}{\sqrt{2\pi}\sigma}e^{-\frac{i^2}{2\sigma^2}}$, $p_{\boldsymbol{\varphi}}^{T,R}(i_1,i_2) = \frac{1}{|\Omega|}\int_\Omega G_\sigma(i_1 - T\circ\boldsymbol{\varphi}(\mathbf{x}), i_2 - R(\mathbf{x}))d\mathbf{x}$, $p^R(i_2) = \int_{-\infty}^{+\infty} p_{\boldsymbol{\varphi}}^{T,R}(i_1,i_2)di_1$, $p_{\boldsymbol{\varphi}}^T(i_1) = \int_{-\infty}^{+\infty} p_{\boldsymbol{\varphi}}^{T,R}(i_1,i_2)di_2$, $\xi,\varpi,\sigma > 0$, and for some small $\varepsilon > 0$, the 2D/3D conformal constraint

$$\begin{aligned} \mathcal{N}_{d,\varepsilon}^M(\Omega) = \{\mathbf{u} = (u_1,\ldots,u_d)^T \in [H_0^\alpha(\Omega)]^d : \|\nabla\varphi_1(\mathbf{x})\|^2 = \cdots = \|\nabla\varphi_d(\mathbf{x})\|^2 \le M^2, \\ det(\nabla\boldsymbol{\varphi}) \ge \varepsilon, \nabla\varphi_i(\mathbf{x})\cdot\nabla\varphi_j(\mathbf{x}) = 0, \qquad \text{for } i\ne j \text{ and } \forall \mathbf{x}\in\Omega\}, \end{aligned} \tag{2.40}$$

$M > 0$, $\boldsymbol{\varphi}(\mathbf{x}) = (\varphi_1(\mathbf{x}),\ldots,\varphi_d(\mathbf{x}))^T \triangleq \mathbf{x} + \mathbf{u}(\mathbf{x})$, $d = 2,3$, the definition of fractional-order derivatives can be found in [18], and the fractional-order α satisfies $\alpha > \left\{\begin{smallmatrix} 2, & d=2, \\ 2.5, & d=3, \end{smallmatrix}\right.$ to ensure $H_0^\alpha(\Omega) \hookrightarrow C^1(\Omega)$ [12, 18], which ensures the derivatives in $\mathcal{N}_{d,\varepsilon}^M(\Omega)$ are well-defined.

Remark 2.6. Here the constraint $\mathcal{N}_{d,\varepsilon}^M(\Omega)$ is used to control the physical mesh folding. In fact, it is equivalent to the Cauchy–Riemann constraint

$$\left\{\mathbf{u} = (u_1,u_2)^T \in [H_0^\alpha(\Omega)]^2 : \frac{\partial u_1}{\partial x_1} = \frac{\partial u_2}{\partial x_2}, \frac{\partial u_1}{\partial x_2} = -\frac{\partial u_2}{\partial x_1}\right\} \tag{2.41}$$

in [21, 23, 24] when $d = 2$ (see Appendix A for details). This constraint makes the numerical implementation for the 2D image registration much easier. An alternative way of imposing diffeomorphism is by adding another and explicit control term in the functional of (2.39) as done in [25, 48, 49, 50].

Concerning the existence of solution to (2.39), we have the following results.

Theorem 2.7. *Assume the discontinuous sets for T and Φ_T ($\Phi = Z,\omega,W$) are all zero measure sets; then there exists at least one solution for* (2.39).

Proof. Selecting a minimizing sequence $\{\mathbf{u}^k\}$ of the functional $\mathcal{K}(\mathbf{u})$, then there holds

$$\int_\Omega |\nabla^\alpha \mathbf{u}^k|^2 d\mathbf{x} \le \frac{1}{\varpi}\mathcal{K}(\mathbf{u}^k) \le \frac{1}{\varpi}\mathcal{K}(\mathbf{0}) < +\infty, \tag{2.42}$$

as k is large enough.

That is, $\{\mathbf{u}^k\}$ is a bounded sequence in $[H_0^\alpha(\Omega)]^d$. By the compactness of $H^\alpha(\Omega)$, there exists a subsequence of $\mathbf{u}^k$ which is still labeled by k and a $\mathbf{u}\in[H^\alpha(\Omega)]^d$ such that $\mathbf{u}^k$ weakly converges to $\mathbf{u}$ with

$$\mathcal{S}(\mathbf{u}) \le \lim_{k\to\infty}\inf \mathcal{S}(\mathbf{u}^k). \tag{2.43}$$

By the compact embedding theorem (Theorem 4.58 in [12]), we know that $H_0^\alpha(\Omega) \hookrightarrow C^1(\Omega)$. Namely, there exists a subsequence of $\mathbf{u}^k$ which is still labeled by k and a $\bar{\mathbf{u}} \in [C^1(\Omega)]^d$ such that $\mathbf{u}^k$ converges to $\bar{\mathbf{u}}$ in $[C^1(\Omega)]^d$. Moreover, by the uniqueness of the limit, we obtain that $\bar{\mathbf{u}} = \mathbf{u}$. That is, $\mathbf{u}^k \xrightarrow{k} \mathbf{u}$ in $[C^1(\Omega)]^d$ and satisfies $\det(\nabla(\mathbf{x}+\mathbf{u}^k)) \xrightarrow{k} \det(\nabla(\mathbf{x}+\mathbf{u})) \ge \varepsilon$ because of the fact that $\det(\nabla(\mathbf{x}+\mathbf{u}^k)) \ge \varepsilon$. Therefore, we conclude that $\mathbf{u}\in\mathcal{N}_{d,\varepsilon}^M(\Omega)$.

In addition, by the fact $\mathbf{u}^k \xrightarrow{k} \mathbf{u}$ in $[C^1(\Omega)]^d$, we have that

$$
\begin{aligned}
p^{T,R}_{\boldsymbol{\varphi}^k}(i_1,i_2) &= \frac{1}{|\Omega|}\int_{\Omega\setminus\triangle_U^k} G_\sigma(i_1 - T\circ\boldsymbol{\varphi}^k(\mathbf{x}), i_2 - R(\mathbf{x}))d\mathbf{x} \\
\xrightarrow{k} p^{T,R}_{\boldsymbol{\varphi}}(i_1,i_2) &= \frac{1}{|\Omega|}\int_{\Omega\setminus\triangle_U} G_\sigma(i_1 - T\circ\boldsymbol{\varphi}(\mathbf{x}), i_2 - R(\mathbf{x}))d\mathbf{x},
\end{aligned} \tag{2.44}
$$

where $\boldsymbol{\varphi}^k(\mathbf{x}) = \mathbf{x} + \mathbf{u}^k(\mathbf{x})$, $\boldsymbol{\varphi}(\mathbf{x}) = \mathbf{x} + \mathbf{u}(\mathbf{x})$, and $\triangle_U^k = (\boldsymbol{\varphi}^k)^{-1}(\triangle_T)$. Note that $\triangle_U^k$ is a zero measure set because of the fact that $\boldsymbol{\varphi}^k : \Omega \to \Omega$ and $(\boldsymbol{\varphi}^k)^{-1} : \Omega \to \Omega$ are bijections ($\mathbf{u}^k \in \mathcal{N}^M_{d,\varepsilon}(\Omega)$ implies $\det(\nabla\boldsymbol{\varphi}^k) > 0$) and $\triangle_T \triangleq \{\mathbf{x} : T(\mathbf{x})$ is discontinuous at $\mathbf{x}\}$ is a zero measure set. Moreover, by the fact $\mathbf{u}^k \xrightarrow{k} \mathbf{u}$ in $[C^1(\Omega)]^d$, we know that $\boldsymbol{\varphi}^k \xrightarrow{k} \boldsymbol{\varphi}$ in $[C^1(\Omega)]^d$. By deduction, $(\boldsymbol{\varphi}^k)^{-1} \xrightarrow{k} \boldsymbol{\varphi}^{-1}$ in $[C^1(\Omega)]^d$ (see Appendix D for details), which implies $\triangle_U^k$ goes to $\triangle_U$ as k goes to infinity, where $\triangle_U = \boldsymbol{\varphi}^{-1}(\triangle_T)$.

Similarly, there holds

$$
p^T_{\boldsymbol{\varphi}^k}(i_1) \xrightarrow{k} p^T_{\boldsymbol{\varphi}}(i_1). \tag{2.45}
$$

By (2.44) and (2.45), we conclude that

$$
\mathcal{M}(\mathbf{u}^k) \xrightarrow{k} \mathcal{M}(\mathbf{u}). \tag{2.46}
$$

Similarly, by the fact that the set $\Delta\Psi_T \triangleq \{\mathbf{x} : \Psi_T(\mathbf{x})$ is discontinuous at $\mathbf{x}\}$ ($\Psi = Z, \omega, W$) are all zero measure sets, and the fact $\mathbf{u}^k \xrightarrow{k} \mathbf{u}$ in $[C^1(\Omega)]^d$, we conclude that

$$
\mathfrak{g}(\mathbf{u}^k) \xrightarrow{k} \mathfrak{g}(\mathbf{u}). \tag{2.47}
$$

By (2.43), (2.46), and (2.47), we obtain $\mathcal{D}(\mathbf{u}^k) \xrightarrow{k} \mathcal{D}(\mathbf{u})$ and

$$
\mathcal{K}(\mathbf{u}) \le \lim_{k\to\infty}\inf \mathcal{K}(\mathbf{u}^k), \tag{2.48}
$$

which ensures the existence of a solution for (2.39). ■

To transform the nonconvexity of $\mathbf{u}$, we introduce a new variable $\mathbf{v}$ to relax $\mathbf{u}$. In a similar way, variable $\mathbf{s}$ is also introduced to address the nonlinear constraint in $\mathcal{N}^M_{d,\varepsilon}(\Omega)$. Based on these new variables, (2.39) is relaxed to the following variational model:

$$
\min_{\mathbf{u}\in[H_0^\alpha(\Omega)]^d, \mathbf{v}\in[L^2(\Omega)]^d, \mathbf{s}\in\mathbb{M}_{d\times d}(L^2(\Omega))} \mathcal{J}(\mathbf{v},\mathbf{u},\mathbf{s}), \tag{2.49}
$$

where $\mathcal{J}(\mathbf{v},\mathbf{u},\mathbf{s}) = \xi\mathcal{D}(\mathbf{v}) + \frac{1}{2\upsilon}\int_\Omega |\mathbf{u}-\mathbf{v}|^2 d\mathbf{x} + \varpi\mathcal{S}(\mathbf{u}) + \Theta\int_\Omega \|\mathbf{s}\mathbf{s}^T - \frac{\|\mathbf{s}\|^2}{d}\mathbf{I}\|^2 d\mathbf{x} + \Upsilon\int_\Omega \|\mathbf{s} - \nabla\boldsymbol{\varphi}\|^2 d\mathbf{x}$, $\upsilon > 0, \Theta > 0, \Upsilon > 0$.

Remark 2.8. In (2.49), $\mathbf{u} \in \mathcal{N}^M_{d,\varepsilon}(\Omega)$. Note that here $\mathcal{N}^M_{d,\varepsilon}(\Omega)$ is used to rule out the deformation $\boldsymbol{\varphi}(\mathbf{x}) = \mathbf{x} + \mathbf{u}$ whose Jacobian determinant is too small. In fact, by setting some large Θ, one can also achieve this goal. To simplify the numerical implementation, we restrict $\mathbf{u}$ to $[H_0^\alpha(\Omega)]^d$ and control $\mathbf{u} \in \mathcal{N}^M_{d,\varepsilon}(\Omega)$ by setting some appropriate Θ.

To solve (2.49), we use the AMM, which splits (2.49) into the following three subproblems:

$$\mathbf{v}^{k+1} = \underset{\mathbf{v}\in[L^2(\Omega)]^d}{\arg\min}\ \mathcal{J}(\mathbf{v},\mathbf{u}^k,\mathbf{s}^k), \tag{2.50}$$

$$\mathbf{u}^{k+1} = \underset{\mathbf{u}\in[H_0^\alpha(\Omega)]^d}{\arg\min}\ \mathcal{J}(\mathbf{v}^{k+1},\mathbf{u},\mathbf{s}^k), \tag{2.51}$$

$$\mathbf{s}^{k+1} = \underset{\mathbf{s}\in\mathbb{M}_{d\times d}(L^2(\Omega))}{\arg\min}\ \mathcal{J}(\mathbf{v}^{k+1},\mathbf{u}^{k+1},\mathbf{s}). \tag{2.52}$$

The sketch of the proof of the convergence of (2.50)–(2.52) under some specific conditions can be divided into two steps: **Step 1**. Show $\{\mathcal{J}(\mathbf{v}^k,\mathbf{u}^k,\mathbf{s}^k)\}$ is a decreasing sequence with respect to k and show $(\mathbf{v}^k,\mathbf{u}^k,\mathbf{s}^k)$ converges to some $(\bar{\mathbf{v}},\bar{\mathbf{u}},\bar{\mathbf{s}})$; **Step 2**. Show $(\bar{\mathbf{v}},\bar{\mathbf{u}},\bar{\mathbf{s}})$ is a minimizer of (2.49). One can use the similar technique of Theorem 3.2 in [21] and Theorem 3.1 in [24] to complete the proof. Here we omit it and focus on the numerical implementation of (2.50)–(2.52).

v-problem (2.50). Define $t_1(\mathbf{u}) = Z_T(\mathbf{x}+\mathbf{u}) - Z_R(\mathbf{x})$, $t_2(\mathbf{u}) = \omega_T(\mathbf{x}+\mathbf{u}) - \omega_R(\mathbf{x})$, $t_3(\mathbf{u}) = W_T(\mathbf{x}+\mathbf{u}) - W_R(\mathbf{x})$, $t_4(\mathbf{u}) = MI(T(\mathbf{x}+\mathbf{u}),R(\mathbf{x}))$; then there holds

$$t_1(\mathbf{v}^{k+1}) \approx t_1(\mathbf{u}^k) + \nabla Z_T(\mathbf{x}+\mathbf{u}^k)\cdot(\mathbf{v}^{k+1}-\mathbf{u}^k), \tag{2.53}$$

$$t_2(\mathbf{v}^{k+1}) \approx t_2(\mathbf{u}^k) + \nabla \omega_T(\mathbf{x}+\mathbf{u}^k)\cdot(\mathbf{v}^{k+1}-\mathbf{u}^k), \tag{2.54}$$

$$t_3(\mathbf{v}^{k+1}) \approx t_3(\mathbf{u}^k) + \nabla W_T(\mathbf{x}+\mathbf{u}^k)\cdot(\mathbf{v}^{k+1}-\mathbf{u}^k), \tag{2.55}$$

$$t_4(\mathbf{v}^{k+1}) \approx t_4(\mathbf{u}^k) + \delta_{\mathbf{u}} MI(T(\mathbf{x}+\mathbf{u}^k),R(\mathbf{x}))\cdot(\mathbf{v}^{k+1}-\mathbf{u}^k). \tag{2.56}$$

Substituting (2.53)–(2.56) into (2.50) yields

$$\mathbf{A}\mathbf{v}^{k+1} = \mathbf{b}^k, \tag{2.57}$$

where $\mathbf{A} = \mathbf{I} + 2\xi\upsilon\mathcal{M}(\mathbf{u}^k)(\delta_Z\mathbf{G}_Z+\delta_\omega\mathbf{G}_\omega+\delta_W\mathbf{G}_W)+2\xi\upsilon\mathfrak{g}(\mathbf{u}^k)\mathbf{G}_M$, $\mathbf{b}^k = -2\xi\upsilon\mathcal{M}(\mathbf{u}^k)[\delta_Z t_1(\mathbf{u}^k)\mathbf{V}_Z - \delta_Z\mathbf{G}_Z\mathbf{u}^k + \delta_\omega t_2(\mathbf{u}^k)\mathbf{V}_\omega - \delta_\omega\mathbf{G}_\omega\mathbf{u}^k + \delta_W t_3(\mathbf{u}^k)\mathbf{V}_W - \delta_W\mathbf{G}_W\mathbf{u}^k] + 2\xi\upsilon\mathfrak{g}(\mathbf{u}^k)[(1-MI(T(\mathbf{x}+\mathbf{u}^k),R(\mathbf{x})))\mathbf{V}_M + \mathbf{G}_M\mathbf{u}^k] + \mathbf{u}^k$, $\mathbf{V}_Z = (\frac{\partial Z_T\circ\boldsymbol{\varphi}^k}{\partial x_1},\dots,\frac{\partial Z_T\circ\boldsymbol{\varphi}^k}{\partial x_d})^T$, $\mathbf{V}_\omega = (\frac{\partial \omega_T\circ\boldsymbol{\varphi}^k}{\partial x_1},\dots,\frac{\partial \omega_T\circ\boldsymbol{\varphi}^k}{\partial x_d})^T$, $\mathbf{V}_W = (\frac{\partial W_T\circ\boldsymbol{\varphi}^k}{\partial x_1},\dots,\frac{\partial W_T\circ\boldsymbol{\varphi}^k}{\partial x_d})^T$. Note that here

$$\mathbf{V}_M = \delta_{\mathbf{u}} MI(T(\mathbf{x}+\mathbf{u}^k),R(\mathbf{x})) = -\frac{1}{|\Omega|}\left(\frac{\partial G_\sigma}{\partial i_1} * L_{\boldsymbol{\varphi}}\right)(T(\mathbf{x}+\mathbf{u}^k),R(\mathbf{x}))\cdot\nabla_{\mathbf{u}}T(\mathbf{x}+\mathbf{u}^k(\mathbf{x})),$$

$L_{\boldsymbol{\varphi}}(i_1,i_2) = 1+\log\frac{p_{\boldsymbol{\varphi}}^{T,R}(i_1,i_2)}{p_{\boldsymbol{\varphi}}^T(i_1)p^R(i_2)}$, $\mathbf{G}_T = \mathbf{V}_T\mathbf{V}_T^T$, $\mathbf{G}_\omega = \mathbf{V}_\omega\mathbf{V}_\omega^T$, $\mathbf{G}_W = \mathbf{V}_W\mathbf{V}_W^T$, $\mathbf{G}_M = \mathbf{V}_M\mathbf{V}_M^T$, and *the derivation for* $\delta_{\mathbf{u}}MI(T(\mathbf{x}+\mathbf{u}^k),R(\mathbf{x}))$ *can be found in Appendix* B.

u-problem (2.51). The associated Euler–Lagrange equation for (2.51) is

$$\begin{cases} \mathcal{L}\mathbf{u}^{k+1} = \mathbf{v}^{k+1} - 2\Upsilon\upsilon\,\mathrm{div}(\mathbf{s}^k), \\ \mathbf{u}^{k+1}(\mathbf{x})|_{\mathbf{x}\in\partial\Omega} = 0, \end{cases} \tag{2.58}$$

where $\mathcal{L} = -2\Upsilon\upsilon\Delta + 2\xi\upsilon\,\mathrm{div}^{\alpha*}(\nabla^\alpha) + \mathbf{I}$ and the definition of the fractional-order operator $\mathrm{div}^{\alpha*}(\nabla^\alpha)$ can be found in [18, 21].

Concerning the numerical implementation of (2.58), one can use the multigrid approach to search for a solution. For $d=2$ and $d=3$, we refer readers to Algorithms 3.1–3.2 in [23] and Algorithm 3.1 in [24], respectively. Since there is no essential difference, we do not repeat it.

s-problem (2.52). Before the numerical implementation of (2.52), let us recall the following lemma in [16].

Lemma 2.9. *Suppose $\mathbf{X}_1$ and $\mathbf{X}_2$ are $d\times d$ ($d=2,3$) matrices, and define*

$$\mathcal{P}(\mathbf{Q}_1,\mathbf{Q}_2)=\|\mathbf{Q}_1^*\mathbf{X}_1\mathbf{Q}_2-\mathbf{X}_2\|^2, \tag{2.59}$$

where $\mathbf{Q}_1,\mathbf{Q}_2$ are $d\times d$ unknown orthogonal matrices, and $\|\cdot\|$ denotes the Frobenius norm.

Let $\mathbf{X}_1=\mathbf{P}_1\mathbf{\Lambda}_1\mathbf{R}_1^*$ and $\mathbf{X}_2=\mathbf{P}_2\mathbf{\Lambda}_2\mathbf{R}_2^*$ be the singular value decomposition (SVD) of $\mathbf{X}_1$ and $\mathbf{X}_2$, respectively. Then the minimizer $\mathbf{Q}_1,\mathbf{Q}_2$ of $\mathcal{P}(\mathbf{Q}_1,\mathbf{Q}_2)$ satisfies

$$\mathbf{P}_1=\mathbf{Q}_1\mathbf{P}_2\mathbf{\Pi},\mathbf{R}_1=\mathbf{Q}_2\mathbf{R}_2\mathbf{\Pi}, \tag{2.60}$$

where $\mathbf{\Pi}$ is the permutation matrices that minimizes $\mathrm{Tr}(\mathbf{\Lambda}_2^*\mathbf{\Pi}^*\mathbf{\Lambda}_1\mathbf{\Pi})$.

At the end of this section, we focus on the problem of how to optimize $\mathbf{s}$ in (2.52). Let $\mathbf{s}(\mathbf{x})\in\mathbb{M}_{d\times d}(L^2(\Omega))$ be defined in (2.52), and assume the SVD of $\nabla\boldsymbol{\varphi}^{k+1}(\mathbf{x})$ is $\nabla\boldsymbol{\varphi}^{k+1}(\mathbf{x})=\mathbf{U}(\mathbf{x})\mathbf{\Lambda}(\mathbf{x})\mathbf{V}^*(\mathbf{x})$, where $\mathbf{\Lambda}(\mathbf{x})\in\mathcal{T}_d$, and $\mathbf{U}(\mathbf{x})$, $\mathbf{V}(\mathbf{x})$ are orthogonal matrices. Then, for any orthogonal matrices $\mathbf{P}(\mathbf{x})$ and $\mathbf{Q}(\mathbf{x})$, define $\mathbf{P}(\mathbf{x})\tilde{\mathbf{\Lambda}}(\mathbf{x})\mathbf{Q}(\mathbf{x})=\mathbf{U}^*(\mathbf{x})\mathbf{s}(\mathbf{x})\mathbf{V}(\mathbf{x})$, where $\tilde{\mathbf{\Lambda}}(\mathbf{x})\in\mathcal{T}_d$ is a diagonal matrix. Note that here $\mathbf{U}(\mathbf{x})$, $\mathbf{V}(\mathbf{x})$ are known matrices and $\mathbf{P}(\mathbf{x})$, $\tilde{\mathbf{\Lambda}}(\mathbf{x})$, $\mathbf{Q}(\mathbf{x})$, and $\mathbf{s}(\mathbf{x})$ are unknown functions for matrix. Based on these facts, $\mathbf{s}(\mathbf{x})$ is optimized if $P,Q,\tilde{\mathbf{\Lambda}}$ are optimized. To achieve this goal, we use Lemma 2.9 to give some results for the $\mathbf{s}$-problem (2.52).

Theorem 2.10. *Let $\mathcal{T}_d$ be a set containing all d-order ($d=2,3$) diagonal matrices, and let $\overline{\mathbf{\Lambda}}$ be the solution of*

$$\min_{\overline{\mathbf{\Lambda}}\in\mathcal{T}_d}\Upsilon\int_\Omega\|\overline{\mathbf{\Lambda}}-\mathbf{\Lambda}\|^2d\mathbf{x}+\Theta\int_\Omega\left\|\overline{\mathbf{\Lambda}}^2-\frac{\|\overline{\mathbf{\Lambda}}\|^2}{d}\mathbf{I}_d\right\|^2d\mathbf{x}. \tag{2.61}$$

Then $\mathbf{U}\overline{\mathbf{\Lambda}}\mathbf{V}^*$ is a minimizer of subproblem (2.52). Here the SVD of $\nabla\boldsymbol{\varphi}^{k+1}$ is $\nabla\boldsymbol{\varphi}^{k+1}=\mathbf{U}\mathbf{\Lambda}\mathbf{V}^*$ and $\mathbf{I}_d$ is d-order ($d=2,3$) identity matrix.

Proof. Based on the above notations, then we know that

$$\mathbf{s}=\mathbf{U}\mathbf{P}\tilde{\mathbf{\Lambda}}\mathbf{Q}\mathbf{V}^*,\ \mathbf{s}\mathbf{s}^T=\mathbf{U}\mathbf{P}\tilde{\mathbf{\Lambda}}^2\mathbf{P}\mathbf{U}^*,\ \|\mathbf{s}\|^2=\|\tilde{\mathbf{\Lambda}}\|^2. \tag{2.62}$$

Substituting (2.62) into (2.52), (2.52) is equivalent to minimizing the following functional:

$$\begin{aligned}\mathcal{P}(\mathbf{P},\tilde{\mathbf{\Lambda}},\mathbf{Q})&=\Theta\int_\Omega\left\|\mathbf{P}(\mathbf{x})\tilde{\mathbf{\Lambda}}^2(\mathbf{x})(\mathbf{x})\mathbf{P}^*(\mathbf{x})-\frac{\|\tilde{\mathbf{\Lambda}}(\mathbf{x})\|^2}{d}\mathbf{I}_d\right\|^2d\mathbf{x}+\Upsilon\int_\Omega\|\mathbf{P}(\mathbf{x})\tilde{\mathbf{\Lambda}}(\mathbf{x})\mathbf{Q}(\mathbf{x})-\mathbf{\Lambda}(\mathbf{x})\|^2d\mathbf{x}\\ &=\Theta\int_\Omega\left\|\tilde{\mathbf{\Lambda}}^2(\mathbf{x})-\frac{\|\tilde{\mathbf{\Lambda}}(\mathbf{x})\|^2}{d}\mathbf{I}_d\right\|^2d\mathbf{x}+\Upsilon\int_\Omega\|\mathbf{P}(\mathbf{x})\tilde{\mathbf{\Lambda}}(\mathbf{x})\mathbf{Q}(\mathbf{x})-\mathbf{\Lambda}(\mathbf{x})\|^2d\mathbf{x}.\end{aligned} \tag{2.63}$$

Note that in (2.62) and (2.63), we use the relationship $\|\mathbf{A}\|^2=\lambda_1+\cdots+\lambda_d$, where λ_i ($i=1,\ldots,d$) are the eigenvalues of $\mathbf{A}\mathbf{A}^T$.

We propose to solve minimizing (2.63) by alternating minimization: first fixing $\tilde{\mathbf{\Lambda}}$ and optimizing (P,Q), and second optimizing $\tilde{\mathbf{\Lambda}}$ based on the optimized (P,Q) in the first step. The process is listed as follows. Fixing $\tilde{\mathbf{\Lambda}}$, then the minimizing problem (2.63) with $(\mathbf{P},\mathbf{Q})$ being unknown functions is of the form of (2.59). Suppose $(\overline{\mathbf{P}},\overline{\mathbf{Q}})$ is the minimizer of $\mathcal{P}(\mathbf{P},\tilde{\mathbf{\Lambda}},\mathbf{Q})$ for some fixed $\tilde{\mathbf{\Lambda}}$. By Lemma 2.9, $\mathbf{I}_d=\overline{\mathbf{P}}\mathbf{\Pi}=\overline{\mathbf{Q}}\mathbf{\Pi}$. Besides, for any orthogonal matrices $\mathbf{P},\mathbf{Q}$ and diagonal matrix $\tilde{\mathbf{\Lambda}}$,

$$
\begin{aligned}
\mathcal{P}(\mathbf{P},\tilde{\mathbf{\Lambda}},\mathbf{Q}) &= \Theta\int_\Omega\left\|\tilde{\mathbf{\Lambda}}^2(\mathbf{x})-\frac{\|\tilde{\mathbf{\Lambda}}(\mathbf{x})\|^2}{d}\mathbf{I}_d\right\|^2 d\mathbf{x}+\Upsilon\int_\Omega\|\mathbf{P}(\mathbf{x})\tilde{\mathbf{\Lambda}}(\mathbf{x})\mathbf{Q}(\mathbf{x})-\mathbf{\Lambda}(\mathbf{x})\|^2 d\mathbf{x}\\
&\ge \Upsilon\int_\Omega\|\mathbf{\Pi}^*\tilde{\mathbf{\Lambda}}(\mathbf{x})\mathbf{\Pi}-\mathbf{\Lambda}(\mathbf{x})\|^2 d\mathbf{x}+\Theta\int_\Omega\left\|\tilde{\mathbf{\Lambda}}^2(\mathbf{x})-\frac{\|\tilde{\mathbf{\Lambda}}(\mathbf{x})\|^2}{d}\mathbf{I}_d\right\|^2 d\mathbf{x}\\
&\ge \Upsilon\int_\Omega\|\tilde{\mathbf{\Lambda}}(\mathbf{x})-\mathbf{\Lambda}(\mathbf{x})\|^2 d\mathbf{x}+\Theta\int_\Omega\left\|\tilde{\mathbf{\Lambda}}^2(\mathbf{x})-\frac{\|\tilde{\mathbf{\Lambda}}(\mathbf{x})\|^2}{d}\mathbf{I}_d\right\|^2 d\mathbf{x}\\
&= \mathcal{P}(\mathbf{I}_d,\tilde{\mathbf{\Lambda}},\mathbf{I}_d) \qquad\qquad \forall\ \tilde{\mathbf{\Lambda}}\in\mathcal{T}_d.
\end{aligned}
\tag{2.64}
$$

That is, $\mathcal{P}(\overline{\mathbf{P}},\tilde{\mathbf{\Lambda}},\overline{\mathbf{Q}})\ge\mathcal{P}(\mathbf{I}_d,\tilde{\mathbf{\Lambda}},\mathbf{I}_d)\ge\mathcal{P}(\mathbf{I}_d,\overline{\mathbf{\Lambda}},\mathbf{I}_d)$ with $\overline{\mathbf{P}}=\overline{\mathbf{Q}}=\mathbf{I}_d$. This concludes $\mathbf{I}_d\overline{\mathbf{\Lambda}}\mathbf{I}_d=\mathbf{U}^*\mathbf{s}\mathbf{V}$ and $\mathbf{s}=\mathbf{U}\overline{\mathbf{\Lambda}}\mathbf{V}^*$. ■

By Theorem 2.10, (2.52) is equivalent to (2.61). Furthermore, by the variational principle [15], the Euler–Lagrange equation of (2.61) for $\overline{\mathbf{\Lambda}}$ is

$$
\Upsilon(\overline{\mathbf{\Lambda}}-\mathbf{\Lambda})+2\Theta\left(\overline{\mathbf{\Lambda}}^2-\frac{1}{d}\|\overline{\mathbf{\Lambda}}\|^2\mathbf{I}_d\right)\overline{\mathbf{\Lambda}}=\mathbf{0}. \tag{2.65}
$$

Letting $\mathbf{\Lambda}=\operatorname{diag}(\kappa_1,\ldots,\kappa_d)$ and $\overline{\mathbf{\Lambda}}=\operatorname{diag}(\sigma_1,\ldots,\sigma_d)$, then (2.65) is equivalent to the following cubic algebraic equations:

$$
\Upsilon(\sigma_i-\kappa_i)+2\Theta\left[\sigma_i^2-\frac{1}{d}\sum_{i=1}^d\sigma_i^2\right]\sigma_i=0,\qquad i=1,\ldots,d. \tag{2.66}
$$

That is,

$$
2\Theta\sigma_i^3+\left[\Upsilon-\frac{2\Theta}{d}\sum_{i=1}^d\sigma_i^2\right]\sigma_i-\Upsilon\kappa_i=0,\qquad i=1,\ldots,d. \tag{2.67}
$$

Here we can write (2.67) as a nonlinear system

$$
\mathbf{g}(\sigma)=\mathbf{0}, \tag{2.68}
$$

where $\mathbf{g}(\sigma)=(g_1(\sigma),\ldots,g_d(\sigma))^T$, $\sigma=(\sigma_1,\ldots,\sigma_d)$, $g_i(\sigma)=\sigma_i^3+p\sigma_i-\frac{1}{d}(\sigma_1^2+\sigma_2^2+\sigma_3^2)\sigma_i-p\kappa_i$ $(i=1,\ldots,d)$, and $p=\frac{\Upsilon}{2\Theta}$.

The Newton's method [2] is used to solve (2.68). After completing the computation of (2.68), the solution of (2.52) is formulated as $\mathbf{s}^{k+1}=\mathbf{U}^*\overline{\mathbf{\Lambda}}\mathbf{V}$.

The numerical implementation for solving (2.49) can be found in Algorithm 2.1.

The overall framework of our proposed three-stage image registration approach is graphically illustrated in Figure 4.

Algorithm 2.1 AMM for 2D/3D multimodality image registration.

Input: region Ω, accuracy, initial error $E=1$, $k=0$, $\lambda, M, \Theta, \Upsilon, \mu$, and maximum iteration times K.
while $E >$accuracy and $k \leq K$
1. Use (2.57) to obtain $\mathbf{v}^{k+1}$;
2. Use (2.58) to obtain $\mathbf{u}^{k+1}$ and $\boldsymbol{\varphi}^{k+1}$;
3. Compute the SVD of $\boldsymbol{\varphi}^{k+1}(\mathbf{x}) = \mathbf{x} + \mathbf{u}^{k+1}(\mathbf{x}) = \mathbf{U}\overline{\mathbf{\Lambda}}\mathbf{V}^*$ and use (2.67) to obtain $\overline{\mathbf{\Lambda}} = \mathrm{diag}(\sigma_1, \ldots, \sigma_d)$;
4. Update $\mathbf{s}^{k+1}$ by setting $\mathbf{s}^{k+1} = \mathbf{U}\overline{\mathbf{\Lambda}}\mathbf{V}^*$;
5. Compute $T(\mathbf{x} + \mathbf{u}^{k+1}(\mathbf{x}))$, registration error $E = \frac{\|T(\cdot + \mathbf{u}^{k+1}(\cdot)) - R(\cdot)\|^2_{L^2(\Omega)}}{\|T(\cdot) - R(\cdot)\|^2_{L^2(\Omega)}}$ and let $k = k+1$;

endwhile
Output: $T(\cdot + \mathbf{u}^k(\cdot))$ for some $k \leq K$.

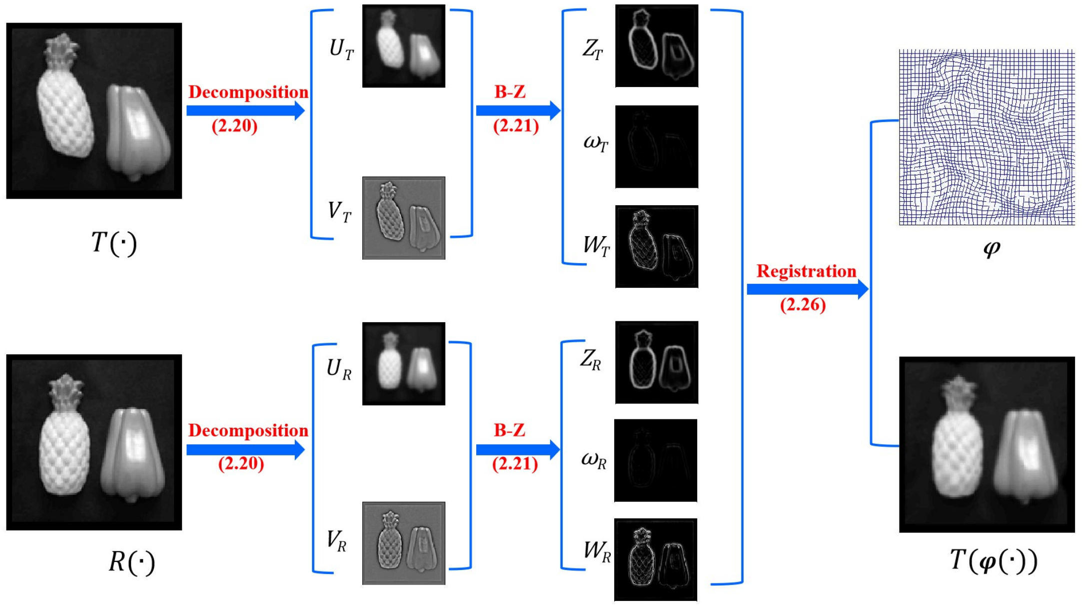

Figure 4. *Framework of the proposed three-stage diffeomorphic multimodality image registration.*

3. Greedy matching for 2D/3D diffeomorphic multimodality model (2.39).

(2.39) pursues the minimizer of $\xi\mathcal{D}(\mathbf{u}) + \varpi\mathcal{S}(\mathbf{u})$, while the ultimate goal for 2D/3D diffeomorphic multimodality image registration is to search for a global minimizer of $\mathcal{D}(\mathbf{u})$ on $\mathcal{N}^M_{d,\varepsilon}(\Omega)$. This is so-called greedy matching, which is formulated as follows:

$$\inf_{\mathbf{u} \in \mathcal{N}^M_{d,\varepsilon}(\Omega)} \mathcal{D}(\mathbf{u}). \tag{3.1}$$

Obviously, (3.1) provides a much more accurate registration result than (2.39). In order to give a more accurate solution for 2D/3D diffeomorphic multimodality image registration, we focus on the numerical implementation for (3.1) in this section. For this purpose, we propose the following coarse-to-fine approach:

I: Downsampling. Given $N \in \mathbb{N}^+$, we downsample the geometric features Ψ_ρ ($\Psi = Z, \omega, W$; $\rho = T, R$) and the image pair $T(\cdot), R(\cdot)$ with size 2^n ($n = 0, 1, 2, \ldots, N$) to obtain the downsampled features Ψ_ρ^n and the image pair $T^n(\cdot), R^n(\cdot)$, respectively.

II: Image registration. Based on the downsampled features Ψ_ρ^n ($\Psi = Z, \omega, W$; $\rho = T, R$; $n = 0, 1, 2, \ldots, N$), we propose a coarse-to-fine approach for solving the greedy matching problem (3.1). The proposed approach is divided into the following $N + 1$ steps, and note that here and in what follows, $\Omega_n = \Omega \downarrow 2^{N-n}$ denotes the downsampling of the region Ω with size 2^{N-n}, for example, giving the region $\Omega = (1, 129)^d$, $\Omega \downarrow 2^1$ denotes the region $(1, 65)^d$):

Step 0. Taking Ψ_ρ^N ($\Psi = Z, \omega, W$; $\rho = T, R$) and the image pair $T^N(\cdot)$, $R^N(\cdot)$ as initial features and image pair, we solve the following variational problem on Ω_0:

$$\mathbf{u}_0 \in \underset{\mathbf{u} \in \mathcal{N}^\infty_{d,\varepsilon_0}(\Omega_0)}{\arg\min} \ \mathcal{K}_0(\mathbf{u}), \tag{3.2}$$

where $\varepsilon_0 > 0$, $\mathcal{K}_0(\mathbf{u}) = \xi_0 \mathcal{D}_{\Omega_0}(\mathbf{u}) + \varpi \mathcal{S}_{\Omega_0}(\mathbf{u})$, $\mathcal{D}_{\Omega_0}(\mathbf{u}) = \mathfrak{g}_{\Omega_0}(\mathbf{u})\mathcal{M}_{\Omega_0}(\mathbf{u})$, $\mathcal{M}_{\Omega_0}(\mathbf{u}) = \|1 - MI(T \circ \boldsymbol{\varphi}(\cdot), R(\cdot))\|^2_{L^2(\Omega_0)}$, $\mathcal{S}_{\Omega_0}(\mathbf{u}) = \int_{\Omega_0} |\nabla^\alpha \mathbf{u}|^2 d\mathbf{x}$. Note that here $\mathcal{D}_{\Omega_0}(\mathbf{u})$, $\mathfrak{g}_{\Omega_0}(\mathbf{u})$, $\mathcal{M}_{\Omega_0}(\mathbf{u})$, and $\mathcal{S}_{\Omega_0}(\mathbf{u})$ are all defined by replacing Ω with Ω_0 in (2.39).

At the end of Step 0, we define $\tilde{\boldsymbol{\varphi}}_0(\mathbf{x}) = \boldsymbol{\varphi}_0(\mathbf{x}) = \mathbf{x} + \mathbf{u}_0(\mathbf{x})$ for each $\mathbf{x} \in \Omega_0$.

Step 1. Scale $\tilde{\boldsymbol{\varphi}}_0(\mathbf{x})$ to Ω_1 and solve the following variational problem on Ω_1 (note that here $|\Omega_1| = 2^d |\Omega_0|$):

$$\mathbf{u}_1 \in \underset{\mathbf{u} \in \mathcal{N}^\infty_{d,\varepsilon_1}(\Omega_1)}{\arg\min} \ \mathcal{K}_1(\mathbf{u}), \tag{3.3}$$

where $\varepsilon_1 > 0$, $\mathcal{K}_1(\mathbf{u}) = \xi_1 \mathcal{D}_{\Omega_1}(\mathbf{u}) + \varpi \mathcal{S}_{\Omega_1}(\mathbf{u})$, $\mathcal{D}_{\Omega_1}(\mathbf{u}) = \mathfrak{g}_{\Omega_1}(\mathbf{u})\mathcal{M}_{\Omega_1}(\mathbf{u})$, here and in what follows, $\mathfrak{g}_{\Omega_n}(\mathbf{u}) = \delta_T \|Z_T^{N-n} \circ \tilde{\boldsymbol{\varphi}}_{n-1}(\cdot + \mathbf{u}(\cdot)) - Z_R^{N-n}(\cdot)\|^2_{L^2(\Omega_n)} + \delta_\omega \|\omega_T^{N-n} \circ \tilde{\boldsymbol{\varphi}}_{n-1}(\cdot + \mathbf{u}(\cdot)) - \omega_R^{N-n}(\cdot)\|^2_{L^2(\Omega_n)} + \delta_W \|W_T^{N-n} \circ \tilde{\boldsymbol{\varphi}}_{n-1}(\cdot + \mathbf{u}(\cdot)) - W_R^{N-n}(\cdot)\|^2_{L^2(\Omega_n)}$, $\mathcal{M}_{\Omega_n}(\mathbf{u}) = \|1 - MI(T^{N-n} \circ \tilde{\boldsymbol{\varphi}}_{n-1}(\cdot + \mathbf{u}(\cdot)), R^{N-n}(\cdot))\|^2_{L^2(\Omega_n)}$.

After finding the solution of (3.3), we define $\boldsymbol{\varphi}_1(\mathbf{x}) = \mathbf{x} + \mathbf{u}_1(\mathbf{x})$ and $\tilde{\boldsymbol{\varphi}}_1(\mathbf{x}) = \tilde{\boldsymbol{\varphi}}_0 \circ \boldsymbol{\varphi}_1(\mathbf{x})$ for each $\mathbf{x} \in \Omega_1$.

Step *N*. Scale $\tilde{\boldsymbol{\varphi}}_{N-1}(\mathbf{x})$ to Ω_N and solve the following variational problem on Ω_N (note that $\Omega_N = \Omega$):

$$\mathbf{u}_N \in \underset{\mathbf{u} \in \mathcal{N}^\infty_{d,\varepsilon_N}(\Omega_N)}{\arg\min} \ \mathcal{K}_N(\mathbf{u}), \tag{3.4}$$

where $\varepsilon_N > 0$, $\mathcal{K}_N(\mathbf{u}) = \xi_N \mathcal{D}_{\Omega_N}(\mathbf{u}) + \varpi \mathcal{S}_{\Omega_N}(\mathbf{u})$.

At last, we define $\boldsymbol{\varphi}_N(\mathbf{x}) = \mathbf{x} + \mathbf{u}_N(\mathbf{x})$ and $\tilde{\boldsymbol{\varphi}}_N(\mathbf{x}) = \tilde{\boldsymbol{\varphi}}_{N-1} \circ \boldsymbol{\varphi}_N(\mathbf{x})$.

Remark 3.1. Three comments are due for (3.2)–(3.4):

(i). In $\mathcal{N}^M_{d,\varepsilon}(\Omega)$, M is only required as a technical requirement to show the convergence of alternating minimization (2.50)–(2.52). In practical implementation, M is replaced by ∞ to simplify the constraints.

(ii). To ensure the coarsest grid contains at least 5 nodes (divided into 4 parts and 3 grids belonging to interior points for finite difference method), total time point N is chosen by $N = \max\{n : \lfloor \frac{N_s}{2^n} \rfloor \leq 4\}$, where N_s is the total number of nodes on x direction and $\lfloor \cdot \rfloor$ is the round down operator.

There is a scaling for $\mathbf{u}_n$ and $\boldsymbol{\varphi}_n$ in each step. To establish the connection between $\boldsymbol{\varphi}_n : \Omega_n \to \Omega_n$ and the final deformation $\boldsymbol{\varphi}_N : \Omega \to \Omega$, we give the following notations for functions $\boldsymbol{\varphi}_n : \Omega_n \to \Omega_n$, $\mathbf{u}^n : \Omega_n \to \mathbb{R}$ and functions $\boldsymbol{\varphi} : \Omega \to \Omega$, $\mathbf{u} : \Omega \to \mathbb{R}$. By the principle of scaling, we define $\boldsymbol{\varphi}(\mathbf{y}) = \boldsymbol{\varphi}^n(\frac{\mathbf{y}}{2^{N-n}})$, $\mathbf{u}(\mathbf{y}) = 2^{N-n}\mathbf{u}^n(\frac{\mathbf{y}}{2^{N-n}})$, where $\mathbf{y} \in \Omega$ and $\mathbf{x} = \mathbf{y}/2^{N-n} \in \Omega_n$. Here, functions $f_n(f = \boldsymbol{\varphi}, \mathbf{u})$ denote the scaled version of the function f on the domain Ω_n. In addition, there also holds $\Psi^n_\rho(\frac{\mathbf{y}}{2^{N-n}}) = \Psi_\rho(\mathbf{y})$ and $\rho^n(\frac{\mathbf{y}}{2^{N-n}}) = \rho(\mathbf{y})$ $(\Psi = Z, \omega, W; \rho = T, R)$.

Using the variable substitution $\mathbf{y} = 2^{N-n}\mathbf{x}$, the variational functional for Step n ($n = 0, 1, 2, \ldots, N$) is reformulated as follows:

$$
\begin{aligned}
\mathcal{K}_n(\mathbf{u}) = \frac{\xi_n}{4^{(N-n)d}} \int_\Omega & \delta_Z[Z_T \circ \tilde{\boldsymbol{\varphi}}_{n-1} \circ \boldsymbol{\varphi}(\mathbf{y}) - Z_R(\mathbf{y})]^2 + \delta_\omega[\omega_T \circ \tilde{\boldsymbol{\varphi}}_{n-1} \circ \boldsymbol{\varphi}(\mathbf{y}) - \omega_R(\mathbf{y})]^2 \\
& + \delta_W[W_T \circ \tilde{\boldsymbol{\varphi}}_{n-1} \circ \boldsymbol{\varphi}(\mathbf{y}) - W_R(\mathbf{y})]^2 d\mathbf{y} \int_\Omega [1 - MI(T \circ \tilde{\boldsymbol{\varphi}}_{n-1} \circ \boldsymbol{\varphi}(\mathbf{y}), R(\mathbf{y}))]^2 d\mathbf{y} \\
& + \frac{\varpi}{4^{(N-n)d}} \mathcal{S}(\mathbf{u}),
\end{aligned} \tag{3.5}
$$

where $\tilde{\boldsymbol{\varphi}}_{-1}(\mathbf{x}) = \mathbf{x}$.

This implies the variational problem in Step n is equivalent to

$$
\mathbf{u}_n \in \underset{\mathbf{u} \in \mathcal{N}^\infty_{d,\varepsilon_n}(\Omega)}{\arg\min}\ \tilde{\mathcal{K}}_n(\mathbf{u}), \tag{3.6}
$$

where $\tilde{\mathcal{K}}_n(\mathbf{u}) = \xi_n \tilde{\mathcal{D}}_n(\mathbf{u}) + \varpi \mathcal{S}(\mathbf{u})$, $\tilde{\mathcal{D}}_n(\mathbf{u}) = \int_\Omega [Z_T \circ \tilde{\boldsymbol{\varphi}}_{n-1} \circ \boldsymbol{\varphi}(\mathbf{y}) - Z_R(\mathbf{y})]^2 + [\omega_T \circ \tilde{\boldsymbol{\varphi}}_{n-1} \circ \boldsymbol{\varphi}(\mathbf{y}) - \omega_R(\mathbf{y})]^2 + [W_T \circ \tilde{\boldsymbol{\varphi}}_{n-1} \circ \boldsymbol{\varphi}(\mathbf{y}) - W_R(\mathbf{y})]^2 d\mathbf{y} \int_\Omega [1 - MI(T \circ \tilde{\boldsymbol{\varphi}}_{n-1} \circ \boldsymbol{\varphi}(\mathbf{y}), R(\mathbf{y}))]^2 d\mathbf{y}$.

By the fact $\tilde{\mathcal{K}}_n(\mathbf{u}^n) \leq \tilde{\mathcal{K}}_n(\mathbf{0})$, we know that $\{\tilde{\mathcal{D}}_n(\mathbf{u}^n)\}$ is a decreasing sequence with lower bound. Define

$$
\delta = \lim_{n \to \infty} \tilde{\mathcal{D}}_n(\mathbf{u}^n) \tag{3.7}
$$

and

$$
\vartheta = \inf\{\mathcal{D}(\mathbf{u}) : \mathbf{u} \in \mathcal{N}^\infty_{d,0}(\Omega)\}; \tag{3.8}
$$

then we have the following results on the relationship between δ and ϑ.

Theorem 3.2. *Let $\boldsymbol{\varphi}_n$ and $\tilde{\boldsymbol{\varphi}}_n$ be defined by (3.2)–(3.4), and suppose $\lim_{n\to+\infty} \varepsilon_n = 0$ and $\lim_{n\to+\infty} \frac{B^{4n-3}\tilde{M}^{4^n}}{\xi_n} = 0$ for some $\tilde{M}, B = B(\Omega) > 1$. Then there holds $\delta = \vartheta$.*

Proof. One can use the similar way of Theorem 2.3 in [23] to give a proof. Since there is no essential different technique compared with the proof of Theorem 2.3 in [23], here we do not repeat it. Note that here $\lim_{n\to+\infty} \varepsilon_n = 0$ is used to ensure $\mathcal{N}^\infty_{d,\varepsilon_n}(\Omega) \xrightarrow{n} \mathcal{N}^\infty_{d,0}(\Omega)$. ∎

Algorithm 3.1 Coarse-to-fine algorithm for the greedy matching (3.1).

Initialization: $n=0$, $\mathbf{u}_n^0=\mathbf{0}$, $\mathbf{v}_n^0=\mathbf{0}$, $\mathbf{s}_n^0=\mathbf{I}_d$, ξ_n $(n=0,1,2,\ldots,N)$, Θ, υ, ϖ, and maximum scale N.
Stage 1. Use (2.5) to obtain the smooth texture (U_T,V_T) and (U_R,V_R) of T, R, respectively;
Stage 2. Set $(U,V)=(U_T,V_T)$ and $(U,V)=(U_R,V_R)$, respectively, and use (2.35) to obtain the homogenized geometric features Ψ_ρ $(\Psi=Z,\omega,W;\ \rho=T,R)$;
Stage 3. **I: Downsampling**: Downsample the geometric features Ψ_ρ $(\Psi=Z,\omega,W;\rho=T,R)$ and the image pair $T(\cdot),R(\cdot)$ with size 2^n to obtain the downsampled features Ψ_ρ^n $(\Psi=Z,\omega,W;\ \rho=T,R;\ n=0,1,2,\ldots,N)$ and the image pair $T^n(\cdot),R^n(\cdot)$, respectively.
II: Image registration:
while $n\le N$
Step 1. Replace Ψ_ρ $(\Psi=Z,\omega,W;\ \rho=T,R)$, $T(\cdot),R(\cdot)$ in (3.9) with Ψ_ρ^{N-n} $(\Psi=Z,\omega,W;\ \rho=T,R)$, $T^{N-n}(\cdot),R^{N-n}(\cdot)$, respectively, and use Algorithm 2.1 to compute $\mathbf{u}_n$ and $\boldsymbol{\varphi}_n$ on Ω_n;
Step 2. Compute $\tilde{\boldsymbol{\varphi}}_n$ on Ω_n;
Step 3. Scale $\tilde{\boldsymbol{\varphi}}_n$ onto a finer domain Ω_{n+1};
Set $n=n+1$;
endwhile
Output: $\tilde{\boldsymbol{\varphi}}_N$ and $T\circ\tilde{\boldsymbol{\varphi}}_N(\cdot)$.

By Theorem 3.2, (3.2)–(3.4) provides a solution to the greedy matching problem (3.1) if ξ_n satisfies the assumptions, and the numerical implementation for (3.2)–(3.4) is approximating (3.6) by replacing $\tilde{\mathcal{D}}(\mathbf{v})$ with $\tilde{\mathcal{D}}_n(\mathbf{v})$ in (2.49). That is,

$$\min_{\mathbf{u}\in[H_0^\alpha(\Omega)]^d,\mathbf{v}\in[L^2(\Omega)]^d,\mathbf{s}\in\mathbb{M}_{d\times d}(L^2(\Omega))}\mathcal{J}_n(\mathbf{v},\mathbf{u},\mathbf{s}),\tag{3.9}$$

where $\mathcal{J}_n(\mathbf{v},\mathbf{u},\mathbf{s})=\xi_n\tilde{\mathcal{D}}_n(\mathbf{v})+\frac{1}{2\upsilon}\int_\Omega|\mathbf{u}-\mathbf{v}|^2d\mathbf{x}+\varpi\mathcal{S}(\mathbf{u})+\Theta\int_\Omega\|\mathbf{s}\mathbf{s}^T-\frac{\|\mathbf{s}\|^2}{d}\mathbf{I}\|^2d\mathbf{x}+\Upsilon\int_\Omega\|\mathbf{s}-\nabla\boldsymbol{\varphi}\|^2d\mathbf{x}$, $\upsilon>0,\Theta>0,\Upsilon>0$.

The details for the numerical implementation of greedy matching (3.1) can be found in Algorithm 3.1.

4. Numerical tests.

In this section, we perform three different kinds of numerical tests to show the good performance of the proposed Algorithm 3.1. In Test 1, we design three experiments to show the advantage of the proposed Algorithm 3.1 on the aspects of antinoise, weak boundary detection, and textural control. The algorithms for numerical comparison involve NGF [17], NNGF [42], MI [29], and Algorithm 3.1. In Test 2, several 2D/3D comparisons between other methods like NGF [17], NNGF [42], MI [29], NCC [31], and our Algorithm 3.1 are performed to show the competitiveness of the proposed Algorithm 3.1. In Test 3, the comparisons for the algorithms NGF [17], MI [29], and NCC [31] and Algorithm 3.1 are performed on a public database (https://www.kaggle.com/datasets/awsaf49/brats20-dataset-training-validation). All the numerical tests are performed under Windows 7 and MATLAB R2012b with an Intel Core i7-6700 CPU @3.40 GHz and 8 GB memory. For the quantitative comparison, we choose the following four indexes:

- MI, which is defined by

$$\mathrm{MI}(T,R,\mathbf{u})=\sum_{i_1,i_2} p_{\boldsymbol{\varphi}}^{T,R}(i_1,i_2)\log\frac{p_{\boldsymbol{\varphi}}^{T,R}(i_1,i_2)}{p^R(i_2)p_{\boldsymbol{\varphi}}^T(i_1)}.$$

- Mesh folding number (MFN), which is defined by

$$\mathrm{MFN}(\mathbf{u})=\sharp\left(\det\overline{J}(\mathbf{u})\leq 0\right),$$

where $\det\overline{J}(\mathbf{u})=(1+\frac{\partial u_1}{\partial x_1})(1+\frac{\partial u_2}{\partial x_2})-\frac{\partial u_1}{\partial x_2}\frac{\partial u_2}{\partial x_1}$ and for any set A, $\sharp(A)$ denotes the number of elements in A.
- $\mathrm{NGFer}(\mathbf{u})$, which is defined by

$$\mathrm{NGFer}(\mathbf{u})=\frac{\mathrm{NGF}(T\circ\boldsymbol{\varphi},R)}{\mathrm{NGF}(T,R)},$$

where $\mathrm{NGF}(T,R)=\int_\Omega 1-[\nabla_n T(\mathbf{x})\cdot\nabla_n R(\mathbf{x})]^2 d\mathbf{x}$, and $\nabla_n\nu(\nu=T,R)$ is the normalized gradient.
- $\mathrm{Dice}(\mathbf{u})$, which is defined by

$$\mathrm{Dice}(\mathbf{u})=2\frac{|T\circ\boldsymbol{\varphi}\bigcap R|}{|T\circ\boldsymbol{\varphi}|+|R|},$$

where $|T\circ\boldsymbol{\varphi}\bigcap R|$ is the total number of pixels that are correctly registered, and $|T\circ\boldsymbol{\varphi}|+|R|$ is the total number of pixels in image registration.

Remark 4.1. In the sense of distribution, the boundary conditions for Stage 1 to Stage 3 are set as follows:

$$U|_{\partial\Omega}=U_0,\frac{\partial^l U}{\partial x_i^l}|_{\partial\Omega}=0\ (l=1,2;i=1,2,\dots,d), V|_{\partial\Omega}=0,\phi|_{\partial\Omega}=0,\mathbf{u}|_{\partial\Omega}=\mathbf{0}. \tag{4.1}$$

4.1. Parameter selection. In Stage 1 to Stage 3, there are many parameters we need to tune. In this subsection, we discuss how to select appropriate parameters for each stage.

Stage 1. In the numerical version (i.e., (2.33)) of the $H^{-1}+H^0+H^2$ decomposition model, the parameter contains α_1, α_2, λ, μ, and β (note that here $\theta=\frac{\mu\lambda}{\beta}$, $\gamma=\mu+\theta$). By the convergence results of (2.33) in Theorem 2.2, there is no additional condition for the convergence result. Therefore, the numerical implementation for Stage 1 is stable (at least holds in a theoretical sense). Based on this fact, one just need to select the parameters to keep the stability of the numerical scheme of the three PDEs in (2.33) (all of the type $-\gamma\Delta U(\mathbf{x})+e(\mathbf{x})U(\mathbf{x})=f(\mathbf{x})$). By our observation, for the most cases, (2.33) produces an accurate decomposition result. Here we recommend the parameters in Stage 1 to be $\alpha_1=1$, $\alpha_2=1$, $\lambda=20$, $\mu=2\times10^{-5}$, $\beta=10^{-5}$. In fact, this parameter selection for Stage 1 keeps unchanged for all the numerical tests in this paper.

Stage 2. The parameters in B-Z homogenization model (2.34) contain τ_i, θ_i $(i=1,2,3)$, and ε. Note that (2.34) is a convex model, and the existence and uniqueness of a solution for each pair of parameters are clear (see Theorem 2.4). By our observation, for most τ_i, θ_i

$(i=1,2,3)$, the model (2.34) works. Here we recommend to set $\tau_i=\theta_i=150$ $(i=1,2,3)$. In addition, by our observation, the parameter ε is very important for model (2.34). Intuitively, for too small ε, Φ_v $(\Phi=Z,\omega,W$ and $v=T,R)$ approaches to a dark image (all intensity equals to 0) which is meaningless for Stage 3. Besides, for too large ε, the features extracted by (2.34) are too rough, and this may also affect the registration in Stage 3. Here ε is recommended to set in interval $[0.005,0.8]$.

Stage 3. The parameters in Stage 3 contain ξ_n, ε_n $(n=0,1,2,\ldots)$, Υ, Θ, υ, and ϖ. Here ε_n is only used in theoretical analysis to rule out the deformation whose Jacobian determinant is too small. In practice, some larger Θ may also help to achieve this goal. Note that Υ, Θ, υ are all coefficients of the penalty term. The selection for these three parameters depends on whether the corresponding term plays a dominant role. For ξ_n, it is necessary to satisfy the greedy matching condition (sufficient and not necessary condition $\lim_{n\to+\infty}\frac{B^{4n-3}\tilde{M}^{4^n}}{\xi_n}=0$) in Theorem 3.2. Here we recommend to set these parameters around $\xi_n = 2020\times 3.2^n$, $\upsilon=1.25\times10^{-5}$, $\Theta=2.3\times10^7$, $\Upsilon=2.3\times10^5$, $\varpi=10^{-3}$.

Remark 4.2. Two factors (parameter and accuracy) may affect the registration result. For the parameters, to ensure the efficiency of the registration algorithm, suitable parameters for Stage 1 and Stage 2 should be selected. Otherwise, it will affect the result of the next stage. For example, in these three stages, the most sensitive parameter is B-Z model (2.34). When ε is too small, the features extracted by the B-Z model are all dark images (intensity is all zeros in the image). This will lead to the wrong deformation in Stage 3 ($\mathbf{u}=\mathbf{0}$ everywhere). For accuracy, to ensure the efficiency of the registration algorithm, the tolerance for accuracy of Stage 1 and Stage 2 should be less than 10^{-2}, which ensures the model in Stage 1and Stage 2 will extract the right feature.

4.2. Test for the noise, weak boundary, and texture control. In this subsection, we perform several numerical tests to validate that the proposed Algorithm 3.1 has an advantage in addressing the registration with intensity inhomogeneity (i.e., noise, weak boundary) and textural structure in multimodality image registration. The test contains three parts—noise, weak boundary, and texture—which will be introduced later, respectively.

Noise. NGF [17] and NNGF [42] are two famous geometric feature based multimodality image registration models. As we know, these two works are sensitive to noise. To validate the fact that the proposed model addresses the registration with noise, we perform two groups of numerical tests. First, to show the fact that the noise has little effect on registration in the proposed algorithm, in Group I, we keep the target image $R(\cdot)$ unchanged and add different levels of Gaussian white noise on the floating image $T(\cdot)$. Second, to validate that the proposed algorithm has the ability to overcome the noise, in Group II, we add different levels of noise on both $T(\cdot)$ and $R(\cdot)$. By using the proposed Algorithm 3.1 to match the image pair with different levels of noise, we give the final results in Figures 5 and 6 and Table 1. By the quantitative comparison result of Group I in Table 1, we see indeed the noise has little effect on the registration result. Furthermore, from the comparison result of Group II in Table 1, we see that the proposed Algorithm 3.1 addresses the multimodality image registration with strong noise. This shows the robustness of the proposed similarity measure $\mathcal{D}(\mathbf{u})$ in model (2.39).

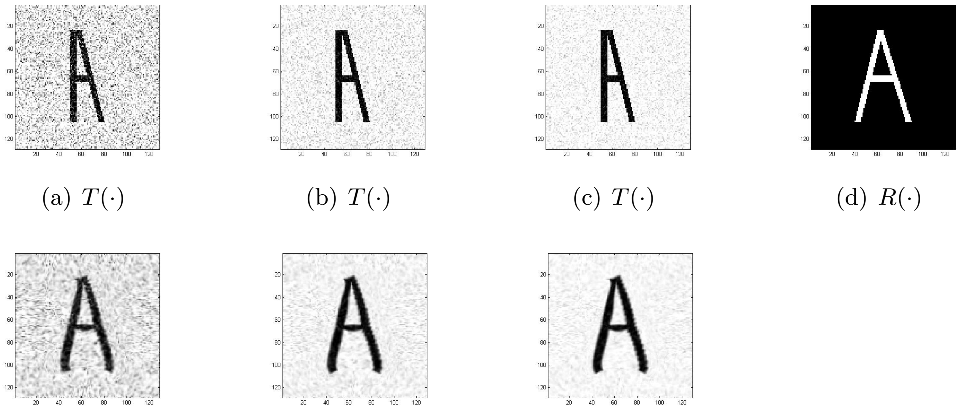

(a) $T(\cdot)$ (b) $T(\cdot)$ (c) $T(\cdot)$ (d) $R(\cdot)$

(e) $T \circ \tilde{\boldsymbol{\varphi}}_N(\cdot)$ (f) $T \circ \tilde{\boldsymbol{\varphi}}_N(\cdot)$ (g) $T \circ \tilde{\boldsymbol{\varphi}}_N(\cdot)$

Figure 5. *Test result for Noise-A-A (Group* I): (a)–(c) *are obtained by adding white Gaussian noise on clean image with standard variance* $\sigma = 80, 36, 25$*, respectively.* (d) *is the target image.* (e)–(g) *are the registration results produced by Algorithm* 3.1 *for* (a)–(c)*, respectively.*

Weak boundary. To validate that the proposed Algorithm 3.1 addresses the multimodality intensity inhomogeneity, the image pairs “square” (Figure 7) and “bone” (Figure 8) are selected for the test data. Weak boundary appears in floating image $T(\cdot)$ and target image $R(\cdot)$ for “square” and only appears in target image $R(\cdot)$ for “bone.” For these two image pairs, Algorithm 3.1 is compared with the NGF [17] and NNGF [42] for multimodality image registration. The final results for the comparison are listed in Figures 7 and 8 and Table 2. From Table 2, we see that the proposed Algorithm 3.1 performs the best among the three multimodality image registration algorithms. In addition, from the aspect of computer vision, we see that Algorithm 3.1 matches the weak boundary well in data “square” and “bone” and produces diffeomorphic deformation, while for NGF [17] and NNGF [42], the failure to detect the weak boundary (see Figure 2(d) for details) leads to the phenomenon that the final results nearly keep unchanged compared with the floating image. Though NNGF [42] improves the NGF [17], it is still not able to match the weak boundary in test data. These results show the competitiveness of the proposed Algorithm 3.1.

Texture. To explain the reason why the textural control is added for registration, we select Pineapple-Pepper (Figure 9) as test data. By observation of Figure 9, one can notice that the texture appears inside the boundary. Obviously, this kind of texture cannot be detected by the first-order and the second-order geometric feature (see Figure 3), let alone NGF and NNGF. Therefore, the final registration results for this image pair provide strong evidence on whether the textural control is helpful for multimodality image registration. In fact, from the quantitative comparison between Algorithm 3.1, NGF [17], and NNGF [42] in Table 2, we see that Algorithm 3.1 outperforms MI [29], NGF [17], and NNGF [42] for image registration with textural structure. In addition, even in Algorithm 3.1, setting $\delta_W = 1$ (textural control, MI $= 2.36$, NGFer $= 0.87$, Dice $= 0.98$) still performs better than the case $\delta_W = 0$ (without textural control, MI $= 2.29$, NGFer $= 0.90$, Dice $= 0.97$). This validates the importance of introducing textural control in multimodality image registration.

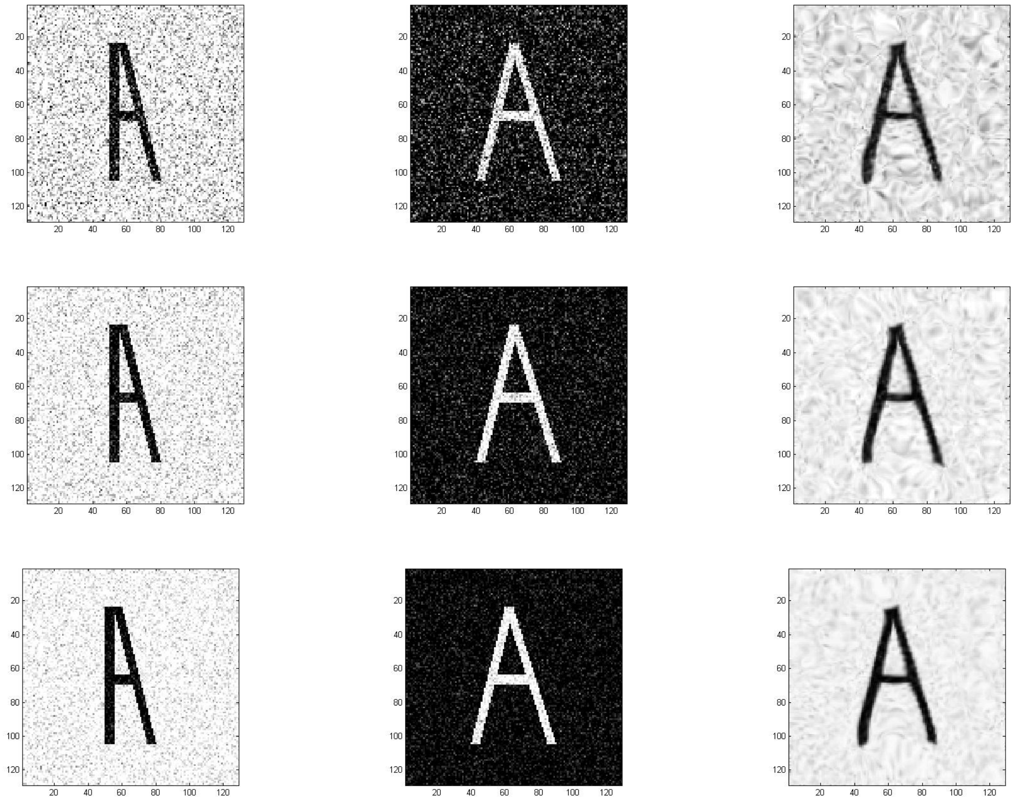

Figure 6. *Test result for Noise-A-A (Group II): The first row is the image $T(\cdot)$, $R(\cdot)$ with Gaussian noise $\sigma = 80$ and the registration result of Algorithm 3.1, respectively; the second row is the image $T(\cdot)$, $R(\cdot)$ with Gaussian noise $\sigma = 36$ and the registration result of Algorithm 3.1, respectively; the third row is the image $T(\cdot)$, $R(\cdot)$ with Gaussian noise $\sigma = 25$ and the registration result of Algorithm 3.1, respectively.*

Table 1
Test for Algorithm 3.1 on antinoise.

	Group I			Group II		
Standard variance	MI	MFN	NGFer	MI	MFN	NGFer
80	0.1449	0	0.9985	0.6858	0	0.9283
36	0.1598	0	0.9916	0.5391	0	0.9188
25	0.1506	0	0.9937	0.4421	0	0.9314

4.3. Test for 2D/3D image registration. To test the performance of Algorithm 3.1 on 2D/3D image registration, we select five different 2D/3D image pairs as test data in this test. For 2D image registration, we select two T1-T2 image pairs (Figure 10(a)–(b) and Figure 11(a)–(b)) as test data. To show the competitiveness of the proposed Algorithm 3.1, we use Algorithm 3.1 and the other state-of-the-art multimodality image registration algorithms

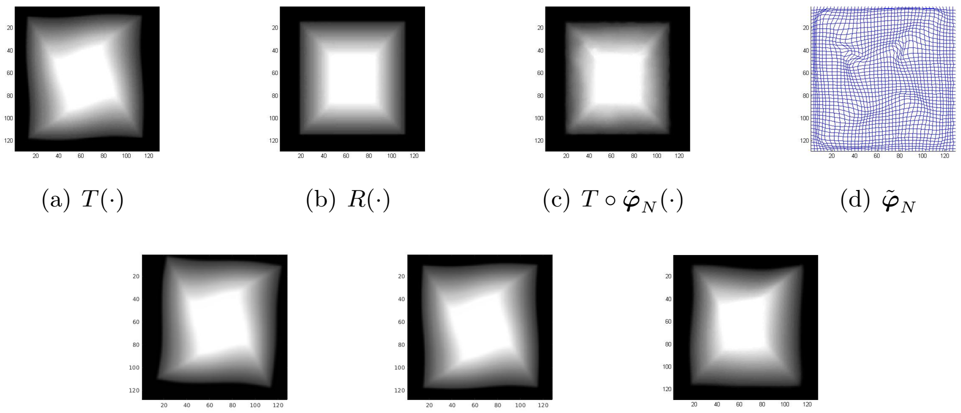

(a) $T(\cdot)$ (b) $R(\cdot)$ (c) $T\circ\tilde{\boldsymbol{\varphi}}_N(\cdot)$ (d) $\tilde{\boldsymbol{\varphi}}_N$

(e) NGF [18] (f) MI [29] (g) NNGF [42]

Figure 7. *Test result for “square” with weak boundary.*

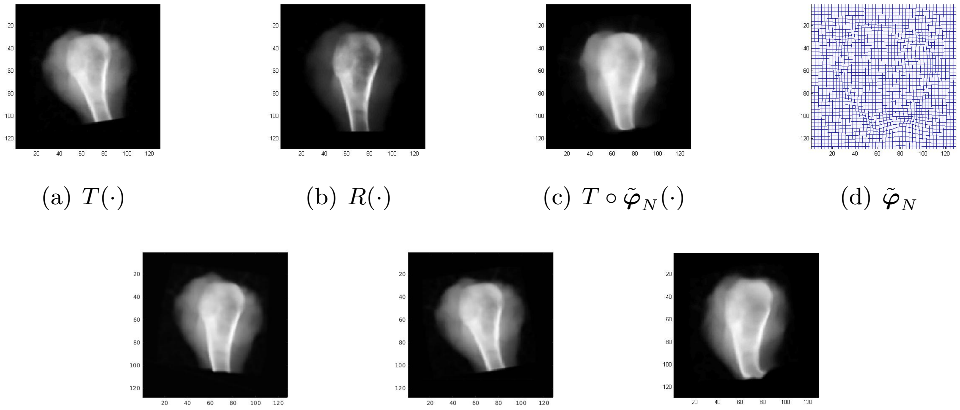

(a) $T(\cdot)$ (b) $R(\cdot)$ (c) $T\circ\tilde{\boldsymbol{\varphi}}_N(\cdot)$ (d) $\tilde{\boldsymbol{\varphi}}_N$

(e) NGF [18] (f) MI [29] (g) NNGF [42]

Figure 8. *Test result for “bone” with intensity inhomogeneity.*

(i.e., NGF [17], NNGF [42], MI [29]) to match these two test image pairs, respectively. The registration results and quantitative comparisons are given in Figures 10 and 11 and Table 3. By Figures 10 and 11, the proposed Algorithm 3.1 matches the test data well and produces diffeomorphic deformation. Besides, the coarse-to-fine approach in Algorithm 3.1 obviously improves the efficiency of the proposed Algorithm 3.1 compared with NGF [17], NNGF [42], and MI [29]. This validates the competitiveness of the proposed Algorithm 3.1.

For 3D image registration, we select one synthetic image pair (Ball-Ellipsoid, 3D; B-E for short), one 3D brain image pair, and one 3D liver image pair as test data. The synthetic image pair is defined as

$$T(\mathbf{x}) = 255\chi_{\Omega\setminus\Omega_1}(\mathbf{x}), R(\mathbf{x}) = 255\chi_{\Omega_2}(\mathbf{x}),$$

Table 2

Test results for image registration with intensity inhomogeneity and textural structure. P-P = Pineapple-Pepper.

	Algorithm	MI	MFN	NGFer	Dice	CPU/s
Square	**Algorithm 3.1**	**2.41**	**0**	**0.83**	**0.99**	**117.5**
	NGF [17]	1.95	0	0.95	0.92	56.8
	NNGF [42]	2.10	0	1.01	0.94	101.9
	MI [29]	1.92	0	0.94	0.92	325.1
Bone	**Algorithm 3.1**	**1.81**	**0**	**0.81**	**0.97**	**82.2**
	NGF [17]	1.59	0	0.99	0.93	42.3
	NNGF [42]	1.61	0	0.94	0.90	103.9
	MI [29]	1.52	0	0.93	0.92	192.1
P-P	**Algorithm 3.1**	**2.36**	**0**	**0.85**	**0.98**	**59.6**
	NGF [17]	1.79	0	1.12	0.90	60.2
	NNGF [42]	2.01	0	1.01	0.95	103.2
	MI [29]	2.05	0	1.01	0.97	200.6

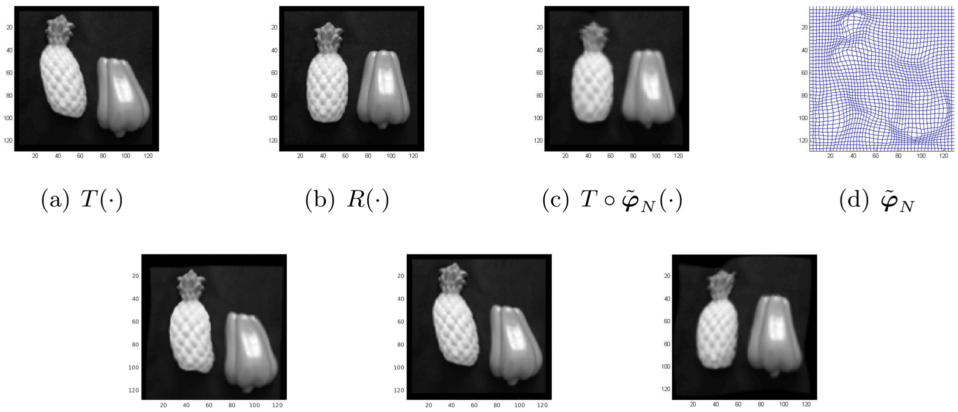

(a) $T(\cdot)$ (b) $R(\cdot)$ (c) $T\circ\tilde{\boldsymbol{\varphi}}_N(\cdot)$ (d) $\tilde{\boldsymbol{\varphi}}_N$

(e) NGF [18] (f) MI [29] (g) NNGF [42]

Figure 9. *Test result for Pineapple-Pepper with textural structure.*

where $\Omega=(1,129)^3$, $\Omega_1=\{\mathbf{x}=(x_1,x_2,x_3)^T:(\frac{x_1-65}{35})^2+(\frac{x_2-65}{35})^2+(\frac{x_3-65}{35})^2\le 1\}$, $\Omega_2=\{\mathbf{x}=(x_1,x_2,x_3)^T:(\frac{x_1-65}{40})^2+(\frac{x_2-65}{35})^2+(\frac{x_3-65}{35})^2\le 1\}$. Note that $\chi_\Omega(\mathbf{x})=1$ if $\mathbf{x}\in\Omega$ and $\chi_\Omega(\mathbf{x})=0$ if $\mathbf{x}$ is not in Ω.

The floating images $T(\cdot)$ for 3D brain and 3D liver are downloaded from the websites [54, 55], respectively. Note here for the convenience of the numerical implementation, we resize all the images into the size $129\times 129\times 129$. In addition, the target images $R(\cdot)$ are generated by $R(\mathbf{x}) = T\circ\boldsymbol{\varphi}(\mathbf{x})$ for any $\mathbf{x} = (x_1,x_2,x_3)^T \in \Omega$, where $\boldsymbol{\varphi}(\mathbf{x})$ is defined by $\boldsymbol{\varphi}(\mathbf{x})=(x_1+u_1(\mathbf{x}),x_2+u_2(\mathbf{x}),x_3+u_3(\mathbf{x}))^T$ and $u_1(\mathbf{x})=3\sin(\frac{2\pi(x_1-1)}{128})$, $u_2(\mathbf{x})=3\sin(\frac{2\pi(x_2-1)}{128})$, $u_3(\mathbf{x})=\sin(\frac{2\pi(x_3-1)}{128})$.

For 3D multimodality image registration, the compared algorithms include Algorithm 3.1, NGF [17], NCC [31], and MI [29]. The final results for the 3D registration are given in Figures 12 to 14 and the quantitative comparison is listed in Table 4. By the quantitative comparison, though it costs much CPU, the proposed Algorithm 3.1 achieves the best

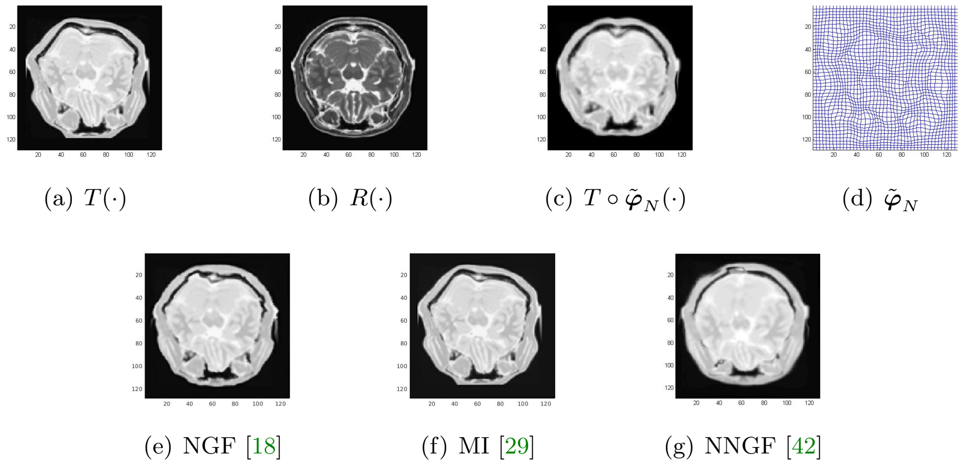

(a) $T(\cdot)$ (b) $R(\cdot)$ (c) $T \circ \tilde{\varphi}_N(\cdot)$ (d) $\tilde{\varphi}_N$

(e) NGF [18] (f) MI [29] (g) NNGF [42]

Figure 10. *Test result for Brain*1.

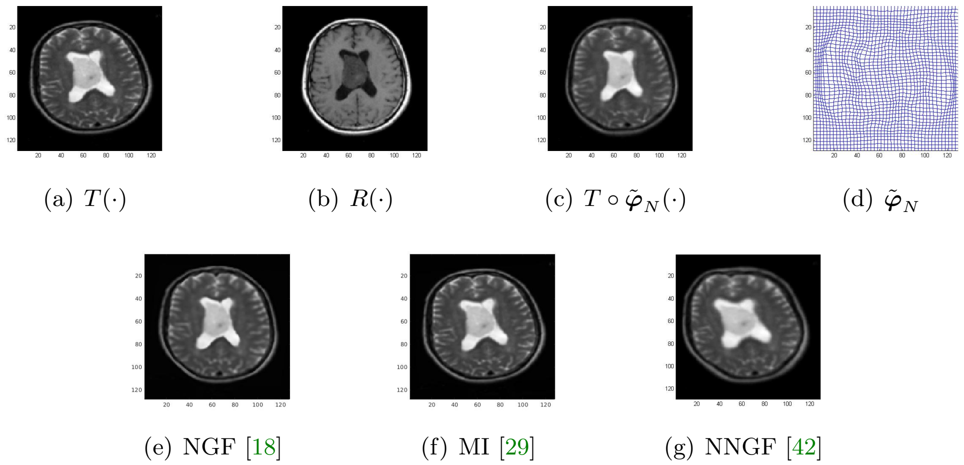

(a) $T(\cdot)$ (b) $R(\cdot)$ (c) $T \circ \tilde{\varphi}_N(\cdot)$ (d) $\tilde{\varphi}_N$

(e) NGF [18] (f) MI [29] (g) NNGF [42]

Figure 11. *Test result for Brain*2.

registration result for the 3D multimodality image. This validates further the competitiveness of the proposed Algorithm 3.1 in addressing the 3D multimodality image registration with intensity inhomogeneity.

4.4. Test for real data on public database. Based on the numerical results in subsections 4.1 and 4.2, there is enough evidence to show that Algorithm 3.1 is competitive. To further validate this conclusion, we select the T1-T2 images in a public database, https://www.kaggle.com/datasets/awsaf49/brats20-dataset-training-validation, for test data. In this public database, the 3D brain images with four different modalities (T1, T1ce, T2, and FLAIR) of 369 subjects are provided. In order to test the advantage for Algorithm 3.1 on addressing the intensity inhomogeneity, we select T1-T2 as test modality, because intensity inhomogeneity is

Table 3

Comparison of four different registration algorithms for $T1$-$T2$ brain images.

	Algorithm	MI	MFN	NGFer	Dice	CPU/s
	Algorithm 3.1	**1.72**	**0**	**0.91**	**0.98**	**21.9**
Brain 1	NGF [17]	1.66	0	0.98	0.98	55.3
	NNGF [42]	1.52	0	1.02	0.93	83.2
	MI [29]	1.55	0	1.01	0.96	196.2
	Algorithm 3.1	**1.47**	**0**	**0.89**	**0.98**	**24.4**
Brain 2	NGF [17]	1.41	0	0.97	0.95	60.1
	NNGF [42]	1.28	0	1.02	0.92	97.0
	MI [29]	1.35	0	0.93	0.93	176.1

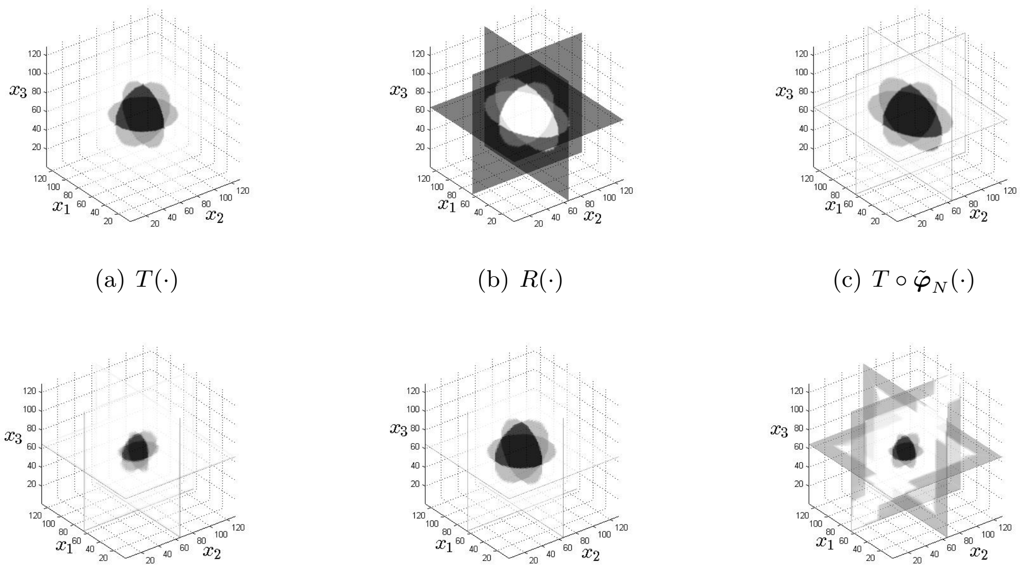

(a) $T(\cdot)$ (b) $R(\cdot)$ (c) $T \circ \tilde{\boldsymbol{\varphi}}_N(\cdot)$

(d) NCC [31] (e) NGF [18] (f) MI [29]

Figure 12. *Test result for 3D-B-E.*

common in the T2 image. Besides, to simplify the test, only 20 different T1-T2 image pairs (the brain structure of 40 different subjects looks most similar) are organized and resized into $129 \times 129 \times 129$ for numerical comparison (the IDs for each image pair are listed in Table 5). The algorithms in quantitative comparison include Algorithm 3.1, NCC [31], NFG [17], and MI [29]. Note that here the algorithms for NCC [31] and NFG [17] are the algorithms for model (57) in [49] by replacing the fidelity SSD with NCC and NFG, respectively. The main parameters for the comparison are $\alpha_1 = 2.6 \times 10^{-11}$, $\alpha_2 = 2.6 \times 10^{-10}$, $\beta = 6.2 \times 10^{-4}$. Concerning the algorithm for MI [29], the test code uses the package "imregister" in MATLAB. Besides, the main parameters in Algorithm 3.1 are set as $\xi_n = 2020 \times 3.2^n$, $\upsilon = 1.25 \times 10^{-5}$, $\Theta = 2.3 \times 10^7$, $\Upsilon = 2.3 \times 10^5$, $\varpi = 10^{-3}$, $\varepsilon = 5 \times 10^{-3}$, $\sigma = 6.5$, $\beta = 10^{-5}$, $\alpha_1 = \alpha_2 = 1$, $\mu = 2 \times 10^{-5}$, $\lambda = 20, \tau_i = \theta_i = 150$ $(i = 1, 2, 3)$, $\delta_Z = \delta_\omega = \delta_W = 1$. The comparison results for

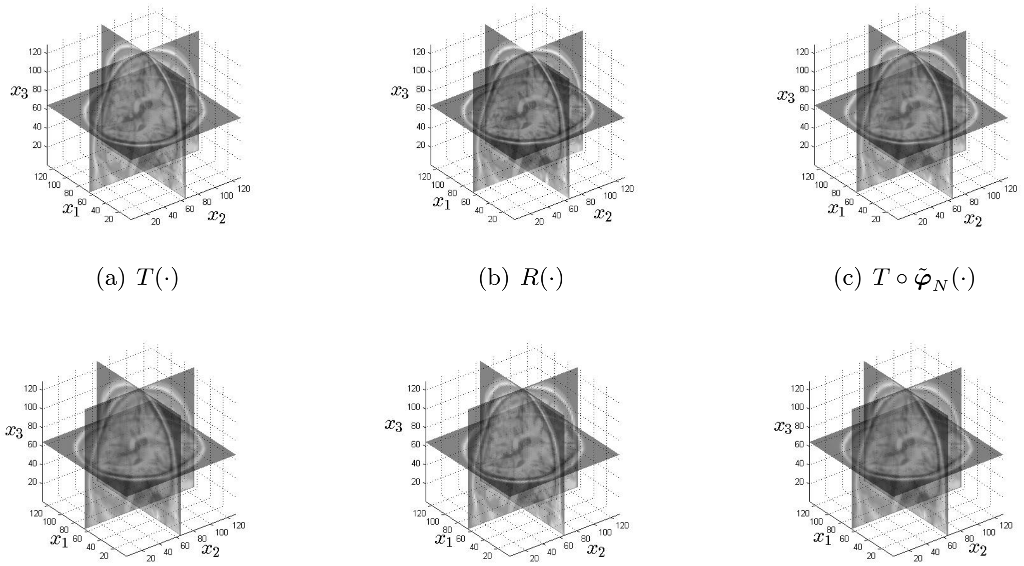

(a) $T(\cdot)$ (b) $R(\cdot)$ (c) $T \circ \tilde{\boldsymbol{\varphi}}_N(\cdot)$

(d) NCC [31] (e) NGF [18] (f) MI [29]

Figure 13. *Test result for 3D-brain.*

the test image pairs are listed in Table 6, where the compared indexes are represented by the mean value $\pm$ standard deviation, respectively.

From Table 6, one can notice that the proposed Algorithm 3.1 achieves the best MI, NGFer, and Dice, though it costs much more CPU time. Therefore, we conclude that the proposed three-stage multimodality image registration outperforms the other three algorithms in the multimodality image registration with intensity inhomogeneity.

5. Conclusion. In this paper, addressing the challenging problem of registering two textured and noisy images in multimodality, the proposed approach solves three variational problems: image decomposition, B-Z homogenization, and image registration. The existence of solutions for these three problems is proved (uniqueness for image decomposition and B-Z homogenization). Moreover, the greedy matching problem is also discussed and a coarse-to-fine algorithm is proposed to search for the global minimizer for the fidelity on a 2D/3D conformal set. Numerical tests are also performed to validate the advantage of the proposed three-stage image registration approach in addressing the intensity inhomogeneity for multimodality image registration. For future research, we hope to address the correction of intensity inhomogeneity in multimodality image registration and give some research on machine learning based registration for multimodality image.

Appendix A. Equivalence between $\mathcal{N}_{2,\varepsilon}^{M}(\Omega)$ and Cauchy–Riemann constraint (2.41). It is obvious that any $\mathbf{u}$ satisfies Cauchy–Riemann constraint (2.41) with $\|\nabla\varphi_1(\mathbf{x})\|^2 = \cdots = \|\nabla\varphi_d(\mathbf{x})\|^2 \leq M^2$ and $\det(\nabla\boldsymbol{\varphi}) \geq \varepsilon$ belongs to the conformal set $\mathcal{N}_{2,\varepsilon}^{M}(\Omega)$, where $\boldsymbol{\varphi}(\mathbf{x}) = (\varphi_1, \varphi_2) = \mathbf{x} + \mathbf{u}(\mathbf{x}) = (x_1 + u_1(\mathbf{x}), x_2 + u_2(\mathbf{x}))$. In this section, for any $\mathbf{u} \in \mathcal{N}_{2,\varepsilon}^{M}(\Omega)$, we claim that $\mathbf{u}$ satisfies Cauchy–Riemann constraint (2.41). The proof is shown as follows.

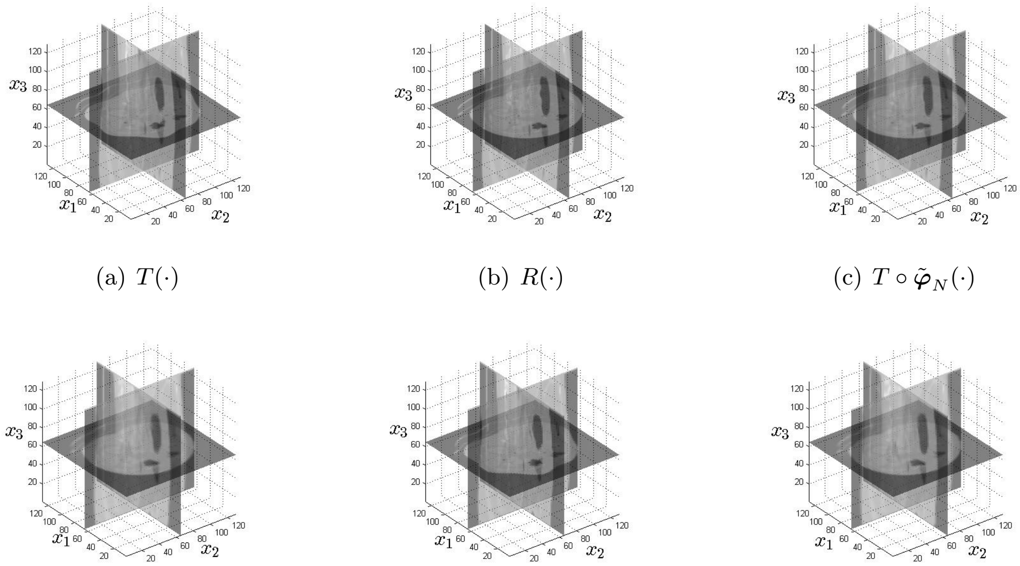

(a) $T(\cdot)$ (b) $R(\cdot)$ (c) $T \circ \tilde{\boldsymbol{\varphi}}_N(\cdot)$

(d) NCC [31] (e) NGF [18] (f) MI [29]

Figure 14. *Test result for 3D-liver.*

Table 4
Comparison of four different registration algorithms for 3D image pairs.

	Algorithm	MI	MFN	NGFer	Dice	CPU/s
3D B-E	**Algorithm 3.1**	**0.49**	**0**	**0.96**	**0.99**	896.1
	NGF [17]	0.32	0	0.99	0.79	7.6
	MI [29]	0.21	0	0.99	0.66	12.3
	NCC [31]	0.13	0	1.01	0.25	13.7
3D Brain	**Algorithm 3.1**	**2.49**	**0**	**0.51**	**0.97**	1974.5
	NGF [17]	1.11	0	0.99	0.93	7.9
	MI [29]	1.31	0	0.94	0.95	12.8
	NCC [31]	2.43	0	0.55	0.97	53.6
3D Liver	**Algorithm 3.1**	**2.35**	**0**	**0.79**	**0.98**	1776.2
	NGF [17]	1.69	0	0.99	0.91	7.8
	MI [29]	1.60	0	0.97	0.91	12.7
	NCC [31]	2.12	0	0.92	0.83	24.1

First, define $\nabla\varphi_1(\mathbf{x}) = (a_1, b_1)$ and $\nabla\varphi_2(\mathbf{x}) = (a_2, b_2)$, where we denote $a_1 = 1 + \frac{\partial u_1}{\partial x_1}$, $b_1 = \frac{\partial u_1}{\partial x_2}$, $a_2 = \frac{\partial u_2}{\partial x_1}$, and $b_2 = 1 + \frac{\partial u_2}{\partial x_2}$ for the convenience of description. By the fact that $\mathbf{u} \in \mathcal{N}_{2,\varepsilon}^M(\Omega)$, we have that

$$\begin{cases} \|\nabla\varphi_1\|^2 = a_1^2 + b_1^2 = \|\nabla\varphi_2\|^2 = a_2^2 + b_2^2, \\ \nabla\varphi_1 \cdot \nabla\varphi_2 = a_1 a_2 + b_1 b_2 = 0, \\ \det(\nabla\boldsymbol{\varphi}) = a_1 b_2 - a_2 b_1 > 0. \end{cases} \tag{A.1}$$

Table 5
Image pair ID.

Pairs	1	2	3	4	5	6	7	8	9	10	11	12	13	14	15	16	17	18	19	20
T1	14	14	103	53	70	95	116	14	114	89	12	14	28	53	99	70	99	12	14	111
T2	114	53	111	114	116	111	120	70	120	114	14	89	111	99	114	114	117	120	116	112

Table 6
Comparison of four different registration algorithms for 3D public database.

Algorithm	MI	MFN	NGFer	Dice	CPU/s
Algorithm 3.1	$\mathbf{0.94 \pm 0.02}$	$\mathbf{0 \pm 0}$	$\mathbf{0.98 \pm 0.01}$	$\mathbf{0.99 \pm 0.01}$	1000.4 ± 24.5
NGF [17]	0.67 ± 0.01	$\mathbf{0 \pm 0}$	$\mathbf{0.99 \pm 0.01}$	$\mathbf{0.94 \pm 0.01}$	$\mathbf{7.2 \pm 0.4}$
MI [29]	0.64 ± 0.02	$\mathbf{0 \pm 0}$	$\mathbf{0.99 \pm 0.00}$	$\mathbf{0.94 \pm 0.01}$	12.8 ± 0.2
NCC [31]	0.74 ± 0.02	$\mathbf{0 \pm 0}$	$\mathbf{0.98 \pm 0.01}$	$\mathbf{0.95 \pm 0.01}$	87.7 ± 16.4

By the second equation in (A.1), we have that

$$\frac{a_1}{b_2} = \frac{-b_1}{a_2} = k \tag{A.2}$$

for some $k : \Omega \to \mathbb{R}$. Note that here k is a function of $\mathbf{x} \in \Omega$, and we write it as k for the convenience of description.

That is,

$$a_1 = kb_2, b_1 = -ka_2. \tag{A.3}$$

Substituting (A.3) into the first equation in (A.1), we obtain that

$$(k^2 - 1)(b_2^2 + a_2^2) = 0 \tag{A.4}$$

for any $\mathbf{x} \in \Omega$.

This yields $k \equiv \pm 1$.

In addition, substituting (A.3) into the third equation in (A.1), we obtain that

$$\det(\nabla \boldsymbol{\varphi}) = k(b_2^2 + a_2^2) > 0. \tag{A.5}$$

This implies $k \equiv 1$.

At last, substituting $k \equiv 1$ into (A.3), there holds

$$\frac{\partial u_1}{\partial x_1} = \frac{\partial u_2}{\partial x_2}, \frac{\partial u_1}{\partial x_2} = -\frac{\partial u_2}{\partial x_1}. \tag{A.6}$$

This concludes the claim.

Appendix B. Derivation of $\partial_{\mathbf{u}} MI(T \circ \varphi, R)$. Define $E(\boldsymbol{\varphi}) = MI(T \circ \boldsymbol{\varphi}, R)$ and let $\mathbf{h}$ be a small perturbation along $\boldsymbol{\varphi}$. Then there holds

$$\begin{aligned} \frac{\partial E(\boldsymbol{\varphi} + \varepsilon \mathbf{h})}{\partial \varepsilon}\Big|_{\varepsilon=0} = & \int_{-\infty}^{+\infty} \int_{-\infty}^{+\infty} \left(1 + \log \frac{p_{\boldsymbol{\varphi}}^{T,R}(i_1, i_2)}{p^D(i_2) p_{\boldsymbol{\varphi}}^T(i_1)} \right) \frac{\partial p_{\boldsymbol{\varphi}+\varepsilon\mathbf{h}}^{T,R}(i_1, i_2)}{\partial \varepsilon}\Big|_{\varepsilon=0} di_1 di_2 \\ & - \int_{-\infty}^{+\infty} \int_{-\infty}^{+\infty} \frac{1}{p_{\boldsymbol{\varphi}}^T(i_1)} p_{\boldsymbol{\varphi}}^{T,R}(i_1, i_2) \frac{\partial p_{\boldsymbol{\varphi}+\varepsilon\mathbf{h}}^T(i_1)}{\partial \varepsilon}\Big|_{\varepsilon=0} di_1 di_2. \end{aligned} \tag{B.1}$$

In addition, by the property of joint probability and marginal probability, there holds

$$\int_{-\infty}^{+\infty} p_{\boldsymbol{\varphi}}^{T,R}(i_1,i_2)di_2 = p_{\boldsymbol{\varphi}}^{T}(i_1) \tag{B.2}$$

and

$$\int_{-\infty}^{+\infty} p_{\boldsymbol{\varphi}}^{T}(i_1)di_1 = 1 \tag{B.3}$$

for any $\boldsymbol{\varphi} \in \mathcal{N}_d^M(\Omega)$.

Using (B.2) and (B.3), we know that the last term in (B.1) can be rewritten as

$$\begin{aligned} &\int_{-\infty}^{+\infty}\int_{-\infty}^{+\infty} \frac{1}{p_{\boldsymbol{\varphi}}^{T}(i_1)} p_{\boldsymbol{\varphi}}^{T,R}(i_1,i_2) \frac{\partial p_{\boldsymbol{\varphi}+\varepsilon\mathbf{h}}^{T}(i_1)}{\partial\varepsilon}|_{\varepsilon=0} di_1 di_2 \\ &= \frac{\partial}{\partial\varepsilon}\int_{-\infty}^{+\infty} p_{\boldsymbol{\varphi}+\varepsilon\mathbf{h}}^{T}(i_1)di_1 = 0. \end{aligned} \tag{B.4}$$

By (B.1) and (B.4), we have that

$$\frac{\partial E(\boldsymbol{\varphi}+\varepsilon\mathbf{h})}{\partial\varepsilon}|_{\varepsilon=0} = \int_{-\infty}^{+\infty}\int_{-\infty}^{+\infty}\left(1+\log\frac{p_{\boldsymbol{\varphi}}^{T,R}(i_1,i_2)}{p^R(i_2)p_{\boldsymbol{\varphi}}^{T}(i_1)}\right)\frac{\partial p_{\boldsymbol{\varphi}+\varepsilon\mathbf{h}}^{T,R}(i_1,i_2)}{\partial\varepsilon}|_{\varepsilon=0}di_1di_2. \tag{B.5}$$

On the other hand, there holds

$$\frac{\partial p_{\boldsymbol{\varphi}+\varepsilon\mathbf{h}}^{T,R}(i_1,i_2)}{\partial\varepsilon}|_{\varepsilon=0} = -\frac{1}{|\Omega|}\int_\Omega \frac{\partial G_\sigma}{\partial i_1}(i_1 - T\circ\boldsymbol{\varphi}(\mathbf{x}), i_2 - R(\mathbf{x}))\nabla_{\mathbf{u}}T\circ\boldsymbol{\varphi}(\mathbf{x})\cdot\mathbf{h}(\mathbf{x})d\mathbf{x}. \tag{B.6}$$

By (B.5) and (B.6), we obtain that

$$\nabla_{\boldsymbol{\varphi}}E = -\frac{1}{|\Omega|}\left(\frac{\partial G_\sigma}{\partial i_1} * L_{\boldsymbol{\varphi}}\right)(T\circ\boldsymbol{\varphi}(\mathbf{x}), R(\mathbf{x}))\nabla_{\mathbf{u}}T\circ\boldsymbol{\varphi}, \tag{B.7}$$

where $L_{\boldsymbol{\varphi}}(i_1,i_2) = 1+\log\frac{p_{\boldsymbol{\varphi}}^{T,R}(i_1,i_2)}{p_{\boldsymbol{\varphi}}^{T}(i_1)p^R(i_2)}$.

Appendix C. Multigrid method for $-\gamma\boldsymbol{\Delta}U(\mathrm{x}) + e(\mathrm{x})U(\mathrm{x}) = f(\mathrm{x})$. Ω is discretized in the following way. For $N \in \mathbb{N}^+$, we define $h = \frac{a}{N}$, $x_{i,p} = ph(i = 1,\dots,d)$ and $\mathbf{x}_{p,\cdot,r} = (x_{1,p},\dots,x_{d,r})$ for $p,r = 0,1,\dots,N$. Using the finite difference method, $-\gamma\Delta U(\mathbf{x}) + e(\mathbf{x})U(\mathbf{x}) = f(\mathbf{x})$ is approximated by the following algebraic equations:

$$\mathcal{L}U = F, \tag{C.1}$$

where for $d=2$, $\mathcal{L}U = -\mathfrak{m}(U_{i+1,j}+U_{i-1,j}+U_{i,j+1}+U_{i,j-1}-4U_{i,j}) + e_{i,j}U_{i,j}$, $F = f_{i,j}$; for $d=3$, $\mathcal{L}U = -\mathfrak{m}(U_{i+1,j,k}+U_{i-1,j,k}+U_{i,j+1,k}+U_{i,j-1,k}+U_{i,j,k+1}+U_{i,j,k-1}-6U_{i,j,k}) + e_{i,j,k}U_{i,j,k}$, $F = f_{i,j,k}$, and $\mathfrak{m} = \frac{\gamma}{h^2}$.

In the multigrid method, one round of V-cycle for finding the solution of (C.1) contains the following four steps:

Step 1. Smoothing. Assume that Ω^h and $\Omega^H (H=2h)$ are the fine grid and coarse grid, respectively. By starting from some initial guess on the finest grid Ω^h and using the 2D/3D solvers

$$U_{\mathbf{x}}^{(\nu+1)} = \frac{E_{m,\mathbf{x}}^{(\nu)}}{F_{m,\mathbf{x}}^{(\nu)}} \tag{C.2}$$

to relax ν_0 times($\nu = 0,1,2,\ldots,\nu_0-1$), we obtain a smooth approximation $\bar{U}^{k+1}$. Note that here for $d=2$, $U_{\mathbf{x}}^{(\nu+1)} = U_{i,j}^{(\nu+1)}$, $E_{m,\mathbf{x}}^{(\nu)} = f_{i,j} + \mathfrak{m}(U_{i+1,j}^{(\nu)} + U_{i-1,j}^{(\nu)} + U_{i,j+1}^{(\nu)} + U_{i,j-1}^{(\nu)})$, $F_{m,\mathbf{x}}^{(\nu)} = 4\mathfrak{m} + e_{i,j}$; for $d=3$, $U_{\mathbf{x}}^{(\nu+1)} = U_{i,j,k}^{(\nu+1)}$, $E_{m,\mathbf{x}}^{(\nu)} = f_{i,j,k} + \mathfrak{m}(U_{i+1,j,k}^{(\nu)} + U_{i-1,j,k}^{(\nu)} + U_{i,j+1,k}^{(\nu)} + U_{i,j-1,k}^{(\nu)} + U_{i,j,k+1}^{(\nu)} + U_{i,j,k-1}^{(\nu)})$, $F_{m,\mathbf{x}}^{(\nu)} = 6\mathfrak{m} + e_{i,j,k}$.

At the end of Step 1, we compute the residual error $\mathbf{r}_{\mathbf{x}}^h$ on Ω^h by

$$\mathbf{r}_{\mathbf{x}}^h = E_{m,\mathbf{x}}^{(\nu_0-1)} - F_{m,\mathbf{x}}^{(\nu_0-1)} U_{\mathbf{x}}^{(\nu_0)}. \tag{C.3}$$

Step 2. Restriction. Compute the residual error on Ω^H by $\mathcal{R}_h^H : \Omega^h \to \Omega^H$

$$\mathbf{r}_{\mathbf{x}}^H = \mathcal{R}_h^H \mathbf{r}_{\mathbf{x}}^h, \tag{C.4}$$

where the definition for $\mathcal{R}_h^H$ is given in [23, 24] in detail.

Next, we relax the equation

$$U_{\mathbf{x}}^{(\nu+1)} = \frac{\bar{E}_{m,\mathbf{x}}^{(\nu)}}{\bar{F}_{m,\mathbf{x}}^{(\nu)}} \tag{C.5}$$

with initial guess $U^{(0)} = \mathbf{0}$ to obtain $\bar{U}^H$. Note that here for $d=2$, $U_{\mathbf{x}}^{(\nu+1)} = U_{i,j}^{(\nu+1)}$, $\bar{E}_{m,\mathbf{x}}^{(\nu)} = f_{i,j} + \mathfrak{m}(U_{i+1,j}^{(\nu)} + U_{i-1,j}^{(\nu)} + U_{i,j+1}^{(\nu)} + U_{i,j-1}^{(\nu)})$, $\bar{F}_{m,\mathbf{x}}^{(\nu)} = 4\mathfrak{m}_H + e_{i,j}$; for $d=3$, $U_{\mathbf{x}}^{(\nu+1)} = U_{i,j,k}^{(\nu+1)}$, $\bar{E}_{m,\mathbf{x}}^{(\nu)} = f_{i,j,k} + \mathfrak{m}_H(U_{i+1,j,k}^{(\nu)} + U_{i-1,j,k}^{(\nu)} + U_{i,j+1,k}^{(\nu)} + U_{i,j-1,k}^{(\nu)} + U_{i,j,k+1}^{(\nu)} + U_{i,j,k-1}^{(\nu)})$, $\bar{F}_{m,\mathbf{x}}^{(\nu)} = 6\mathfrak{m}_H + e_{i,j,k}$, and $\mathfrak{m}_H = \frac{\gamma}{H^2}$.

At the end of Step 1, we compute the residual error $\mathbf{r}_{\mathbf{x}}^h$ on Ω^h by

$$\mathbf{r}_{\mathbf{x}}^h = \bar{E}_{m,\mathbf{x}}^{(\nu_0-1)} - \bar{F}_{m,\mathbf{x}}^{(\nu_0-1)} \bar{U}_{\mathbf{x}}^H. \tag{C.6}$$

Step 3. Coarsest grid solution. On coarsest grid Ω^H, the linear system

$$\mathcal{L}U = F \tag{C.7}$$

is accurately solved.

By solving the linear equations (C.7), U^H is updated.

Step 4. Interpolation. Now we use U^H to correct the approximations on the finer grid Ω^h by the following 2D/3D interpolation operator $\mathcal{I}_H^h : \Omega^H \to \Omega^h$, which is defined by

$$U^h = \mathcal{I}_H^h U^H, \tag{C.8}$$

where the definition for $\mathcal{I}_H^h$ is given in [23, 24] in detail.

Using U^h as an initial guess, we relax (C.2) ν times and repeat the interpolation, correction, and smoothing process until the algorithm reaches the finest grid Ω^h. Finally, relax (C.2) with initial guess U^h to obtain the solution U^h for this round of the V-cycle.

Iterating several times using the V-cycle, one can obtain the solution of $-\gamma\Delta U(\mathbf{x}) + e(\mathbf{x})U(\mathbf{x}) = f(\mathbf{x})$.

Appendix D. Uniform convergence of $(\varphi^k)^{-1} \to \varphi^{-1}$ on $[C^1(\Omega)]^d$. First, for any $\mathbf{u} \in \mathcal{N}_{d,\varepsilon}^M(\Omega)$ and $\varphi(\mathbf{x}) = \mathbf{x} + \mathbf{u}(\mathbf{x})$, there holds

$$m \triangleq d\varepsilon^{\frac{d}{2}} \leq d[\det(\nabla\varphi)]^{\frac{d}{2}} \leq \|\nabla\varphi\|_F^2 \leq 3M^2 \triangleq \bar{M} \tag{D.1}$$

and

$$\nabla\varphi\nabla^T\varphi = \|\nabla\varphi\|_F^2\mathbf{I}. \tag{D.2}$$

Note that here we use the property $\|\nabla\varphi\|_F^2 \geq d[\det(\nabla\varphi)]^{\frac{d}{2}}$ of $\mathcal{N}_{d,\varepsilon}^M(\Omega)$ in [49].

Based on the fact that $\mathbf{u}^k \in \mathcal{N}_{d,\varepsilon}^M(\Omega)$ and (D.1)–(D.2), there holds

$$m \leq \|\nabla\varphi^k\|_F^2 \leq \bar{M} \quad \forall k \tag{D.3}$$

and

$$\nabla\varphi^k\nabla^T\varphi^k = \|\nabla\varphi^k\|_F^2\mathbf{I}. \tag{D.4}$$

By the fact $\varphi^k : \Omega \to \Omega$ and $\varphi : \Omega \to \Omega$ are bijections, for any $\mathbf{y} \in \Omega$, there exists unique $\mathbf{x}, \mathbf{x}^k$ such that $\mathbf{y} = \varphi(\mathbf{x}) = \varphi^k(\mathbf{x}^k)$. Then

$$|\varphi^k(\mathbf{x}^k) - \varphi^k(\mathbf{x})| = |\varphi(\mathbf{x}) - \varphi^k(\mathbf{x})| \to 0 \qquad \forall \mathbf{x} \in \Omega, \tag{D.5}$$

as $k \to +\infty$, because $\varphi^k \to \varphi$ in $[C^1(\Omega)]^d$.

By (D.5) and the fact that $(\varphi^k)^{-1} \in [C^1(\Omega)]^d$, we have that, for any $\mathbf{y} \in \Omega$,

$$|(\varphi^k)^{-1}(\mathbf{y}) - \varphi^{-1}(\mathbf{y})| = |\mathbf{x}^k - \mathbf{x}| = |(\varphi^k)^{-1}(\varphi^k(\mathbf{x}^k)) - (\varphi^k)^{-1}(\varphi^k(\mathbf{x}))| \to 0, \tag{D.6}$$

as k goes to infinity.

Furthermore, by the fact $\mathbf{x} = \varphi^{-1}(\varphi(\mathbf{x}))$, we have $\mathbf{I} = \nabla_{\mathbf{y}}\varphi^{-1}(\mathbf{y}) \cdot \nabla_{\mathbf{x}}\varphi(\mathbf{x})$.

Therefore, by (D.2), we obtain that

$$\nabla_{\mathbf{y}}\varphi^{-1}(\mathbf{y}) = [\nabla_{\mathbf{x}}\varphi(\mathbf{x})]^{-1} = \frac{1}{\|\nabla\varphi\|_F^2}\nabla_{\mathbf{x}}^T\varphi(\mathbf{x}). \tag{D.7}$$

Similarly, there holds

$$\nabla_{\mathbf{y}}(\varphi^k)^{-1}(\mathbf{y}) = \frac{1}{\|\nabla\varphi^k\|_F^2}\nabla_{\mathbf{x}^k}^T\varphi^k(\mathbf{x}^k). \tag{D.8}$$

Combining (D.7)–(D.8), we obtain that

$$\begin{aligned}
&|\nabla_{\mathbf{y}}(\varphi^k)^{-1}(\mathbf{y}) - \nabla_{\mathbf{y}}\varphi^{-1}(\mathbf{y})| = \left|\frac{1}{\|\nabla\varphi^k\|_F^2}\nabla_{\mathbf{x}^k}^T\varphi^k(\mathbf{x}^k) - \frac{1}{\|\nabla\varphi\|_F^2}\nabla_{\mathbf{x}}^T\varphi(\mathbf{x})\right| \\
&= \left|\frac{\|\nabla\varphi\|_F^2\nabla_{\mathbf{x}^k}^T\varphi^k(\mathbf{x}^k) - \|\nabla\varphi^k\|_F^2\nabla_{\mathbf{x}}^T\varphi(\mathbf{x})}{\|\nabla\varphi^k\|_F^2\|\nabla\varphi\|_F^2}\right| = \left|\frac{\|\nabla\varphi\|_F^2\nabla_{\mathbf{x}^k}^T\varphi(\mathbf{x}) - \|\nabla\varphi^k\|_F^2\nabla_{\mathbf{x}}^T\varphi(\mathbf{x})}{\|\nabla\varphi^k\|_F^2\|\nabla\varphi\|_F^2}\right| \\
&\leq \left|\frac{\|\nabla\varphi\|_F^2[\nabla_{\mathbf{x}^k}^T\varphi(\mathbf{x}) - \nabla_{\mathbf{x}}^T\varphi(\mathbf{x})]}{\|\nabla\varphi^k\|_F^2\|\nabla\varphi\|_F^2}\right| + \left|\frac{[\|\nabla\varphi\|_F^2 - \|\nabla\varphi^k\|_F^2]\nabla_{\mathbf{x}}^T\varphi(\mathbf{x})}{\|\nabla\varphi^k\|_F^2\|\nabla\varphi\|_F^2}\right| \\
&\leq \frac{1}{m^2}[\bar{M}|\nabla_{\mathbf{x}^k}^T\varphi(\mathbf{x}) - \nabla_{\mathbf{x}}^T\varphi(\mathbf{x})| + \|\varphi\|_{C^1(\Omega)}|\|\nabla\varphi\|_F^2 - \|\nabla\varphi^k\|_F^2|] \to 0,
\end{aligned} \tag{D.9}$$

as k goes to infinity. Note that here we use the fact $|\mathbf{x}-\mathbf{x}^k| \xrightarrow{k} 0$ (see (D.6) for details), $\boldsymbol{\varphi}^k \xrightarrow{k} \boldsymbol{\varphi}$ in $[C^1(\Omega)]^d$, and $H_0^\alpha(\Omega) \hookrightarrow C^1(\Omega)$ [12, 18] to ensure $\|\boldsymbol{\varphi}\|^2_{[C^1(\Omega)]^d} \le (\|\mathbf{x}\|_{[C^1(\Omega)]^d} + \|\mathbf{u}(\cdot)\|_{[C^1(\Omega)]^d})^2 \le \hat{M}$, where $\|\mathbf{u}(\cdot)\|^2_{[C^1(\Omega)]^d} \le C\|\mathbf{u}(\cdot)\|^2_{[H_0^\alpha(\Omega)]^d} \le C\mathcal{K}(\mathbf{0})$.

Based on (D.6) and (D.9), we conclude that $(\boldsymbol{\varphi}^k)^{-1}$ uniformly converges to $\boldsymbol{\varphi}^{-1}$ on Ω with $\|(\boldsymbol{\varphi}^k)^{-1} - \boldsymbol{\varphi}^{-1}\|_{[C^1(\Omega)]^d} \to 0$ as k goes to infinity.

Acknowledgment. The authors of this paper would like to thank two referees for their very helpful remarks.

REFERENCES

[1] A. Blake and A. Zisserman, *Visual Reconstruction*, MIT Press, Cambridge, MA, 1987.
[2] R. Burden and J. D. Faires, *Numerical Analysis*, Brooks, Boston, 2011.
[3] M. Burger, J. Modersitzki, and L. Ruthotto, *A hyperelastic regularization energy for image registration*, SIAM J. Sci. Comput., 35 (2013), pp. B132–B148, https://doi.org/10.1137/110835955.
[4] L. Burrows, A. Theljani, and K. Chen, *On a variational and convex model of the Blake-Zisserman type for segmentation of low-contrast and piecewise smooth images*, J. Imaging, 7 (2021), 228, https://doi.org/10.3390/jimaging7110228.
[5] M. Carriero, A. Leaci, and F. Tomarelli, *A survey on the Blake-Zisserman functional*, Milan J. Math., 83 (2015), pp. 397–420, https://doi.org/10.1007/s00032-015-0246-x.
[6] A. Chambolle and P. L. Lions, *Image recovery via total variation minimization and related problems*, Numer. Math., 76 (1997), pp. 167–188, https://doi.org/10.1007/s002110050258.
[7] Y. Chen, J. Shi, M. Rao, and J. Lee, *Deformable multi-modal image registration by maximizing Rényi's statistical dependence measure*, Inverse Probl. Imaging, 9 (2015), pp. 79–103, https://doi.org/10.3934/ipi.2015.9.79.
[8] N. Chumchob, *Vectorial total variation-based regularization for variational image registration*, IEEE Trans. Image Process., 22 (2013), pp. 4551–4559, https://doi.org/10.1109/TIP.2013.2274749.
[9] N. Chumchob, K. Chen, and C. Loeza, *A fourth-order variational image registration model and its fast multi grid algorithm*, Multiscale Model. Simul., 9 (2011), pp. 89–128, https://doi.org/10.1137/100788239.
[10] J. B. Conway, *A Course in Functional Analysis*, Springer, New York, 2007.
[11] N. Debroux, C. Le Guyader, and L. A. Vese, *A multiscale deformation representation*, SIAM J. Imaging Sci., 16 (2023), pp. 802–841, https://doi.org/10.1137/22M1510200.
[12] F. Demengel, G. Demengel, and R. Erne, *Functional Spaces for the Theory of Elliptic Partial Differential Equations*, Springer, London, 2012, https://link.springer.com/book/10.1007/978-1-4471-2807-6.
[13] Z. Ding and H. Han, *Two-dimensional diffeomorphic model for multi-modality image registration*, Comput. Appl. Math., 42 (2023), 17, https://doi.org/10.1007/s40314-022-02145-1.
[14] M. Droske and M. Rumpf, *A variational approach to nonrigid morphological image registration*, SIAM J. Appl. Math., 64 (2003), pp. 668–687, https://doi.org/10.1137/S0036139902419528.
[15] L. Evans, *Partial Differential Equations*, AMS, Providence, RI, 2010, https://doi.org/10.1090/gsm/019.
[16] J. Gower and G. B. Dijksterhuis, *Procrustes Problems*, Oxford University Press, Oxford, UK, 2004.
[17] E. Haber and J. Modersitzki, *Intensity gradient based registration and fusion of multi-modal images*, Methods Inf. Med., 46 (2007), pp. 292–299, https://doi.org/10.1007/11866763_89.
[18] H. Han, *A variational model with fractional-order regularization term arising in registration of diffusion tensor image*, Inverse Probl. Imaging, 12 (2018), pp. 1263–1291, https://doi.org/10.3934/ipi.2018053.
[19] H. Han, *A tensor voting based fractional-order image denoising model and its numerical algorithm*, Appl. Numer. Math., 145 (2019), pp. 133–144, https://doi.org/10.1016/j.apnum.2019.06.010.
[20] H. Han and A. Wang, *A fast multi grid algorithm for 2D diffeomorphic image registration model*, J. Comput. Appl. Math., 394 (2021), 113567, https://doi.org/10.1016/j.cam.2021.113576.
[21] H. Han and Z. Wang, *A diffeomorphic image registration model with fractional-order regularization and Cauchy–Riemann constraint*, SIAM J. Imaging Sci., 13 (2020), pp. 1240–1271, https://doi.org/10.1137/19M1260621.

[22] H. Han and Z. Wang, *3D diffeomorphic image registration with Cauchy-Riemann constraint and lower bounded deformation divergence*, ESAIM Math. Model. Numer., 57 (2023), pp. 299–328, https://doi.org/10.1051/m2an/2022080.

[23] H. Han, Z. Wang, and Y. Zhang, *Multiscale approach for two-dimensional diffeomorphic image registration*, Multiscale Model. Simul., 19 (2021), pp. 1538–1572, https://doi.org/10.1137/20M1383987.

[24] H. Han, Z. Wang, and Y. Zhang, *Multiscale approach for three-dimensional conformal image registration*, SIAM J. Imaging Sci., 15 (2022), pp. 1431–1468, https://doi.org/10.1137/21M1455929.

[25] C. Huang, K. Chen, M. Huang, D. Kong, and J. Yuan, *Topology-preserving image registration with novel multi-dimensional Beltrami regularization*, Appl. Math. Model., 125 (2024), pp. 539–556, https://doi.org/10.1016/j.apm.2023.09.033.

[26] M. Ibrahim, K. Chen, and C. Brito-Loeza, *A novel variational model for image registration using Gaussian curvature*, Geom. Imaging Comput., 1 (2014), pp. 417–446, https://doi.org/10.4310/GIC.2014.v1.n4.a2.

[27] K. C. Lam and L. M. Lui, *Landmark- and intensity-based registration with large deformations via quasi-conformal maps*, SIAM J. Imaging Sci., 7 (2013), pp. 2364–2392, https://doi.org/10.1137/130943406.

[28] L. M. Lui and T. C. Ng, *A splitting method for diffeomorphism optimization problem using Beltrami coefficients*, J. Sci. Comput., 63 (2015), pp. 573–611, https://doi.org/10.1007/s10915-014-9903-4.

[29] F. Maes, A. Collignon, D. Vandermeulen, G. Marchal, and P. Suetens, *Multimodality image registration by maximization of mutual information*, IEEE Trans. Med. Imaging., 16 (1997), pp. 187–198, https://doi.org/10.1109/42.563664.

[30] Y. Meyer, *Oscillating Patterns in Image Processing and Nonlinear Evolution Equations*, Univ. Lecture Ser. 22, AMS, Providence, RI, https://doi.org/10.1090/ulect/022.

[31] J. Modersitzki, *FAIR: Flexible Algorithms for Image Registration*, SIAM, Philadelphia, 2009.

[32] D. Mumford and B. Gidas, *Stochastic models for generic images*, Quart. Appl. Math., 59 (2001), pp. 85–111, https://doi.org/10.1093/qjmath/52.1.127.

[33] D. Mumford and J. Shah, *Optimal approximations by piecewise smooth functions and associated variational problems*, Comm. Pure Appl. Math., 42 (1989), pp. 577–685, https://doi.org/10.1002/cpa.3160420503.

[34] S. Osher, S. Andres, and L. Vese, *Image decomposition and restoration using total variation minimization and the $H1$ norm*, Multiscale Model. Simul., 1 (2003), pp. 349–370, https://doi.org/10.1137/S1540345902416247.

[35] J. Pluim, J. Maintz, and M. Viergever, *Image registration by maximization of combined mutual information and gradient information*, IEEE Trans. Med. Imaging., 19 (2000), pp. 809–814, https://doi.org/10.1109/42.876307.

[36] D. Qiu, K.-C. Lam, and L.-M. Lui, *Computing quasi-conformal folds*, SIAM J. Imaging Sci., 12 (2019), pp. 1392–1424, https://doi.org/10.1137/18M1220042.

[37] D. Qiu and L. M. Lui, *Inconsistent surface registration via optimization of mapping distortions*, J. Sci. Comput., 83 (2020), pp. 1–31, https://doi.org/10.1007/s10915-020-01246-5.

[38] L. Rudin, S. Osher, and E. Fatemi, *Nonlinear total variation based noise removal algorithms*, Phys. D, 60 (1992), pp. 259–268, https://doi.org/10.1016/0167-2789(92)90242-F.

[39] M. Rumpf and B. Wirth, *A nonlinear elastic shape averaging approach*, SIAM J. Imaging Sci., 2 (2009), pp. 800–833, https://doi.org/10.1137/080738337.

[40] M. Rumpf and B. Wirth, *Variational Methods in Shape Analysis*, Springer, New York, 2015, https://doi.org/10.1007/978-1-4939-0790-8_56.

[41] J. Shen, *Piecewise $H^{-1}+H^0+H^1$ images and the Mumford-Shah-Sobolev model for segmented image decomposition*, Appl. Math. Res. Express, 4 (2005), pp. 143–167, https://doi.org/10.1155/AMRX.2005.143.

[42] A. Theljani and K. Chen, *An augmented Lagrangian method for solving a new variational model based on gradients similarity measures and high order regulariation for multimodality registration*, Inverse Probl. Imaging, 2 (2019), pp. 309–335, https://doi.org/10.3934/ipi.2019016.

[43] L. Vese and S. Osher, *Modeling textures with total variation minimization and oscillating patterns in image processing*, J. Sci. Comput., 1 (2003), pp. 85–111, https://doi.org/10.1023/A:1025384832106.

[44] B. Wirth, *On the Gamma-limit of joint image segmentation and registration functionals based on phase fields*, Interfaces Free Bound., 18 (2016), pp. 441–477, https://doi.org/10.4171/IFB/370.

[45] F. Wu and C. Desoer, *Global inverse function theorem*, IEEE Trans. Circuit Theory, 19 (1972), pp. 199–201, https://doi.org/10.1109/TCT.1972.1083429.

[46] C. P. Yung, G. Choi, K. Chen, and L. M. Lui, *Efficient feature-based image registration by mapping sparsified surfaces*, J. Vis. Commun. Image R., 55 (2018), pp. 561–571, https://doi.org/10.1016/j.jvcir.2018.07.005.

[47] M. Zanetti, V. Ruggiero, and M. Miranda Jr, *Numerical minimization of a second-order functional for image segmentation*, Commun. Nonlinear Sci. Numer. Simul., 36 (2016), pp. 528–548, https://doi.org/10.1016/j.cnsns.2015.12.018.

[48] D. Zhang and K. Chen, *A novel diffeomorphic model for image registration and its algorithm*, J. Math. Imaging Vision, 2018 (2018), pp. 1–30, https://doi.org/10.1007/s10851-018-0811-3.

[49] D. Zhang and K. Chen, *3D orientation-preserving variational models for accurate image registration*, SIAM J. Imaging Sci., 13 (2020), pp. 1653–1691, https://doi.org/10.1137/20M1320006.

[50] D. Zhang, G. P. T. Choi, J. Zhang, and L. M. Lui, *A unifying framework for n-dimensional quasi-conformal mappings*, SIAM J. Imaging Sci., 15 (2022), pp. 960–988, https://doi.org/10.1137/21M1457497.

[51] D. Zhang, A. Theljani, and K. Chen, *Multi-modality image registration models and efficient algorithms*, Math. Methods Image Process. Inverse Problems, 360 (2018), pp. 33–60, https://doi.org/10.1007/978-981-16-2701-9_3.

[52] J. Zhang and K. Chen, *Variational image registration by a total fractional-order variation model*, J. Comput. Phys., 293 (2015), pp. 442–461, https://doi.org/10.1016/j.jcp.2015.02.021.

[53] J. Zhang, K. Chen, and B. Yu, *A novel high-order functional based image registration model with inequality constraint*, Comput. Math. Appl., 72 (2016), pp. 2887–2899, https://doi.org/10.1016/j.camwa.2016.10.018.

[54] *BrainWeb: Simulated Brain Database*, https://brainweb.bic.mni.mcgill.ca/brainweb/, 2013.

[55] 3*d-ircadb*-02, https://www.ircad.fr/research/data-sets/respiratory-cycle-3d-ircadb-02/, 2019.